

OPTICAL AND NEAR-INFRARED COLOR PROFILES IN NEARBY EARLY-TYPE GALAXIES AND THE IMPLIED AGE AND METALLICITY GRADIENTS

HONG WU^{1,6}, ZHENGYI SHAO^{2,6}, H. J. MO^{3,6}, XIAOYANG XIA⁴, ZUGAN DENG⁵

hwu@bao.ac.cn

ABSTRACT

We present results of an age and metallicity gradient analysis inferred from both optical and near-infrared surface photometry. The analysis is based on a sample of 36 nearby early-type galaxies, obtained from the Early Data Release of the Sloan Digital Sky Survey and the Two Micron All Sky Survey. Surface brightness profiles were derived in each band, and used to study the color gradients of the galaxies. Using simple stellar population models with both optical and near infrared colors, we may interpret the color gradients in term of age and metallicity gradients of galaxies. Using $g_Z \equiv d \log Z_{\text{met}} / d \log R$ and $g_A = d \log \text{Age} / d \log R$ to represent the metallicity and age gradients, we found a median value of $g_Z = -0.25 \pm 0.03$ for the metallicity gradient, with a dispersion $\sigma_{g_Z} = 0.19 \pm 0.02$. The corresponding values for the age gradients were $g_A = 0.02 \pm 0.04$ and $\sigma_{g_A} = 0.25 \pm 0.03$. These results are in good agreement with recent observational results, as well as with recent simulations that suggest both monolithic collapse and major mergers have played important roles in the formation of early-type galaxies. Our results demonstrate the potential of using multi-waveband colors obtained from current and future optical and infrared surveys in constraining the age and metallicity gradients of early-type galaxies.

Subject headings: galaxies: photometry - galaxies: metallicity - galaxies: age

¹National Astronomical Observatories, CAS, Beijing 100012, P.R. China

²Shanghai Astronomical Observatory, CAS, Shanghai 200030, P.R. China

³Astronomy Department, University of Massachusetts, Amherst MA 01003, USA

⁴Department of Physics, Tianjin Normal University, Tianjin 300074, P. R. China

⁵College of Physical Sciences, Graduate School of the Chinese Academy of Sciences, P.O. Box 3908, Beijing 100039, P. R. China

⁶Max-Planck-Institute für Astrophysik, Karl Schwarzschild Str. 1, Postfach 1317, 85741 Garching, Germany

1. INTRODUCTION

The color gradients of early type galaxies have been known for quite a long time (de Vaucouleurs 1961; Boroson, Thompson & Shectman 1983). Such gradients are believed to be due to the variation of the properties of the underlying stellar population, such as age and metallicity. Theoretically, radial variations in metallicity are expected in some formation scenarios for early-type galaxies. For example, early simulations of the monolithic collapse of a gas cloud tended to predict metallicity gradients that are too steep to match observations (e.g. Larson 1974; Carlberg 1984). Later simulations based on mergers of gas-rich galaxies predict that interactions between merging galaxies can effectively dampen their metallicity gradients (e.g. White 1980; Kobayashi 2004). Moreover, radial age gradients are also theoretically conceivable. Therefore, detailed color gradient data are essential to discriminate different formation models of early-type galaxies.

Spectroscopic indices are the most commonly used indicators of metallicity in early-type galaxies. Earlier measurements indicate the existence of systematic metallicity gradients at the level $\Delta \log Z / \Delta \log R \approx -0.1$ to -0.3 (Baum, Thomsen, & Morgan 1986; Carollo, Danziger, and Buson 1993; Davies, Sadler, & Peletier 1993; Henry & Worthey 1999; Mehlert et al. 2000 and 2003). However, it is not easy to obtain a large sample using this technique, because of the difficulties associated with observing long-slit (two-dimensional) spectra. In addition, the rapid decrease of surface brightness with radius limits the radial range over which accurate spectroscopic measurements can be obtained. Such measurements are usually possible only out to a radius of about one or two effective radius, making it difficult to study gradients in the outer part of early-type galaxies.

On the other hand, broad band surface photometry with CCD is relatively easy to expand the measurements to several effective radius. Furthermore, radial profiles obtained from surface photometry are an average measurement within an isophotic annulus, and so are a better representation of the average properties at a given radius. With modern telescopes, accurate multi-waveband photometry can be obtained with little difficulty for a large number of galaxies, making it possible to study the gradients of the stellar population in a statistical way. Because of these reasons, photometric measurements are also widely used for studying the metallicity and age gradients in early-type galaxies, although the interpretation of such measurements has to contend with the well-known age-metallicity degeneracy (e.g. Worthey 1994). Early analyses of nearby galaxies in optical bands all indicated that early-type galaxies have systematic color gradients (Boroson, Thompson, & Shectman 1983; Davis et. al. 1985; Cohen 1986; Franx, Illingworth, & Heckman 1989; Peletier et al. 1990; Michard 1999; Scodéglio 2001; Idiart, Michard, & de Freitas Pacheco 2002). This is supported by the more recent analysis of the surface photometry of E/S0 galaxies in the nearby rich cluster Abell

2199 by Tamura & Ohta (2003).

Because of the age-metallicity degeneracy, the observed color gradients are usually interpreted either as the metallicity gradients or the age gradients, assuming the gradients of the other quantity is known. Assuming the age of the stellar population to be the same over an entire galaxy, both Peletier, Valentijn, & Jameson (1990) and Idiart, Michard, & de Freitas Pacheco (2003) obtained a metallicity gradient of ~ -0.16 (in terms of $\Delta \log Z / \Delta \log R$). Under the same assumption, Tamura & Ohta (2003) found an average metallicity gradient of -0.3 ± 0.1 from a sample of 40 galaxies in Abell 2199 and 11 galaxies in Abell 2634. Using stellar population synthesis models, Saglia et al. (2000) examined the origin of the observed color gradients by comparing the 20 brightest early-type galaxies in CL0949+44, a cluster at a redshift of ~ 0.4 taken from HST WF2 frames, with local galaxies. They concluded that their results are better explained in terms of passive evolution of metallicity gradients than pure age gradients. Hinkley & Im (2001) investigated the optical and near-infrared color gradients in the HST WFPC2 and NICMOS images for six field early-type galaxies with redshifts from 0.4 to 1.0. By comparing with stellar synthesis models, they found that 5 out of the 6 galaxies show negligible age gradients and are dominated by a metallicity gradient. Similarly, Mehlert et al. (2003) found nearly zero age gradients in 35 early-type galaxies in the Coma cluster. However, Silva & Elston (1994) investigated both the optical and near-infrared color gradients in eight early-type galaxies and found that all of them show both metallicity and age gradients. Therefore, whether the color gradients can be ascribed to pure metallicity gradients is still controversial.

As pointed out by de Jong (1996; see also Cardiel et al. 2003; MacArthur et al. 2004), the age-metallicity degeneracy may be partially broken by adding infrared photometry to the optical colors. Including infrared data also has another advantage, since contamination by dust is expected to be less important in infrared than in optical. Thus, accurate near infrared photometry are extremely useful in studying stellar population gradients in galaxies.

In this paper, we use the broad band photometry obtained by the Sloan Digital Sky survey (SDSS) in the optical, together with the 2 Micron All Sky Survey (2MASS) photometric data in the near-infrared, to study the color gradients for nearby early-type galaxies. The relative high image quality in both the SDSS and 2MASS surveys makes it possible to trace the spectral energy distribution (SED) to the outer part of individual galaxies. In addition, since the combined SDSS and 2MASS data give a uniform coverage of the SEDs over a large wavelength range, we may hope to use such data to derive stringent constraints on the variations of the stellar populations in early-type galaxies. As we will show, although 2MASS images are shallower and have lower resolution than the SDSS images, the S/N is sufficient for probing the color gradients to more than 2 effective radii. In this paper, we

present results based on 36 early-type galaxies. Although this sample is not larger than those used in early analyses, this is the first time where SEDs from both optical and near infrared are used to study the stellar population gradients. As we will see, the results we obtain are in good agreement with those obtained from line indices measurements, which demonstrates the strength of combining optical and near infrared photometry in constraining the stellar population gradients in early-type galaxies. In the future, much larger samples can be obtained, making this approach a very promising one for such study.

The outline of this paper is as follows. We describe our galaxy sample and related data reduction in section 2. In sections 3 and 4 we examine the color gradients of these galaxies, and use stellar population synthesis models to obtain constraints on their age and metallicity gradients. We discuss our results in section 5 and give a summary of our results in section 6. Except where stated otherwise, we assume the Hubble constant to be $H_0 = 70 \text{ km s}^{-1} \text{ Mpc}^{-1}$.

2. SAMPLE AND DATA REDUCTION

2.1. The Sample

The sample of early-type galaxies used in this work was selected from the Early Data Release (EDR. Stoughton et al. 2002) of the SDSS, which covers about 462 deg^2 of the sky. Nearby galaxies that are brighter than 13.5 magnitude in the r -band were selected, which guarantees that all the sample galaxies are bright and large enough to be measured in their outer regions in all SDSS and 2MASS bands. Since one of the main goals of this work was to use broad-band photometry to disentangle the age-metallicity effects in observed color gradients, accurate photometric measurements are required. Total 36 early-type galaxies of E and S0 type were selected out. Most of the morphological types were obtained from the literature (RC3 of de Vaucouleurs et al. 1991; NASA/IPAC Extragalactic Database; Nakamura et al. 2003). The remaining galaxies were classified with morphological types by inspecting their SDSS images and radial profiles. Since no other selection criteria were used except the above mentioned magnitude limit, the sample is roughly a magnitude-limited unbiased sample of early-type galaxies. All the galaxies have absolute B magnitudes between -19 and -23 with the narrow $B - V$ color range of 0.9 to 1.1. Table 1 lists all sample galaxies, their redshifts, morphological types from different sources, and absolute magnitudes in the B -band (which was deduced from the SDSS g -images together with the color correction given in eq. [3]).

For each of the sample galaxies, corrected images in the five SDSS bands (u, g, r, i and z) were extracted from the EDR archive imaging frames, which are produced by the SDSS

pipeline with both photometric and astrometric calibrations (Stoughton, 2002). Each frame contains 2048×1489 pixels, and the size of each pixel is $0.396''$. The typical 1σ background noise is 27.4, 28.3, 27.9, 27.3 and 25.9 mag arcsec $^{-2}$ for u , g , r , i and z , respectively. Near-infrared images in the J ($1.25\mu\text{m}$), H ($1.65\mu\text{m}$), and K_S ($2.17\mu\text{m}$) bands were extracted from the 2MASS 2nd data release (Cutri et al. 2000) according to the SDSS coordinates. In our analysis the uncompressed atlas images provided by this data release were used. The pixel size of all of the 2MASS images was $1''$. The typical 1σ background noise we obtained was 21.5, 20.6 and 19.9 mag arcsec $^{-2}$ J , H and K_S , respectively, in agreement with that given in Jarrett et al. (2003).

2.2. Data Reduction

2.2.1. Preliminary Data Processing of the EDR Images

Image processing in the five SDSS bands was originally performed by the photometric pipeline (PHOTO), which performs tasks such as labelling frame artifacts (bad columns, cosmic rays, bleed trails), bias subtraction, and flat-field correction. The astrometric solutions for all the five bands were obtained from the astrometric pipeline (ASTROM) with typical errors much smaller than $0.1''$ (Stoughton et al. 2002). The astrometric accuracy of 2MASS is better than $0.2''$ (Cutri et al. 2000). Thus the images in any 2 bands of the SDSS and 2MASS could be matched very well.

Although the images from the SDSS archive were processed with photometric corrections, some spurious features were still present in many image frames, especially in the u and z bands. The spatial variation of these features was about 1 to 2 ADU. For galaxies which happen to be located in such features, the variation was found to affect both background subtraction and the measurement of color profiles in the outer parts of the image, where the surface brightness is low. Fortunately, most of these features were only one dimensional, and the variation was only along horizontal lines. Thus it was not difficult to measure and then pick them out from images. To do this, firstly a region was selected that includes several hundred lines, covers all columns but does not contain any bright objects. The median of these lines was then measured and used to represent the features. Finally, the high order Spline3 function was used to fit the median line, and features were removed from each line of the image. Figure 1 shows an example of such spurious features in a u -band image. The upper two panels show plots of the average of 500 lines in two different parts of the CCD frame. The left panel shows lines 1 to 500, while the right panel shows lines 971 to 1470. As one can see, the features in both panels are quite similar, indicating that these features are quite systematic through the whole CCD frame. The lower two panels show the same

Table 1: A sample of 36 early-type galaxies from the SDSS EDR.

object	redshift	M_B mag(Vega)	RC3 ^a	NFY ^b	NED ^c	this work ^d
ARK402	0.0178	-20.01		1		
ARK404	0.0187	-19.84		0		
CGCG010-030	0.0392	-21.32	0 S0/a	0	E	
CGCG390-020	0.0374	-21.11				S0
GIN060	0.0443	-20.28			E	
IC0590-1	0.0203	-19.69		0	E	
IC0590-2	0.0209	-19.81		1	E	
IC0891	0.0216	-20.16		0		
IC1517	0.0245	-20.63				S0
IC1639	0.0180	-20.08			cE	
NGC0078b	0.0183	-19.79	-2 S0		S0 ⁰ pec?	
NGC0359	0.0178	-20.11	-2 S0		S0-:	
NGC0364	0.0170	-20.17	-2 S0		(R)SB(s)0 ⁰	
NGC0426	0.0175	-20.19	-4 E	0	E+	
NGC0430	0.0177	-20.56	-5 E		E:	
NGC0867	0.0213	-20.84	0 S0/a		S0+:	
NGC0934	0.0212	-20.37	-2 S0		SAB0-	
NGC0936	0.0048	-20.48	-1 S0-S0/a		SB(rs)0+	
NGC3325	0.0189	-20.75	-5 E		E:	
NGC4044	0.0205	-20.48	-3 E-S0		E+:	
NGC4493	0.0232	-20.51	-4 E	0	E+ pec:	
NGC5865	0.0391	-21.83	-2 S0		SAB0-	
NGC5869	0.0070	-19.65	-2 S0		S0 ⁰ :	
NGC6319	0.0275	-21.05				S0
NGC6359	0.0099	-19.45	-2 S0		SA0-:	
NGC6382	0.0295	-21.00				E
NGC6391	0.0276	-20.51				E
NGC7684	0.0171	-20.35	0 S0/a		S0+	
UGC00588	0.0443	-21.67	0 S0/a		E	
UGC00599	0.0436	-21.52			E/S0	
UGC00797	0.0449	-21.56			cD;E:	
UGC01072	0.0172	-19.63	-2 S0		S0	
UGC05515	0.0443	-22.29	-4 E		E+ pec:	
UGC06435	0.0254	-20.95	-2 S0	0	S0 ⁰ :	
UGC07177	0.0203	-19.99	-3 E-S0	0	S0-?	
UGC07813	0.0232	-20.67	-5 E	0	E:	

^aThird Reference Catalogue of Bright Galaxies, de Vaucouleurs et al. 1991

^bNakamura et al. 2003; Here, 0: E; 1: S0

^cNASA/IPAC Extragalactic Database

^dDetermined by both morphology and radial profile

plots as in the upper panels, except that the spurious features are now subtracted. One can see that the patterns are removed quite successfully by our method. In most cases, the subtraction method reduced the spatial variation to a level ~ 0.2 ADU. The subtraction method failed to suppress the variation to such a low level only for a few very large galaxies and for images with heavily saturated stars, where it is difficult to find a sufficiently large blank-line region to estimate the median value.

2.2.2. *Surface Photometry*

The FWHMs of the SDSS PSFs ($\sim 1.5''$) are much smaller than those of the 2MASS ($\sim 2.5''$). Therefore the SDSS images were downgraded by convolving with a proper Gaussian kernel to match the 2MASS PSFs, in order that SEDs for the inner regions of the galaxies could be obtained with a similar seeing in different bands. Note that the SDSS PSF may change slightly from band to band, and the kernel used is in accordance with the specific filter and field in consideration. To obtain the true surface brightness profiles, an accurate sky background subtraction is essential. For a given galaxy, all other objects in the frame were masked using SExtractor (Bertin & Arnouts 1996). Since most of the sample galaxies have sizes of only a few arcmins, a region of sky sufficient to fit the sky background reasonably well could easily be found.

The ISOPHOTE package in IRAF was used to fit each of the sky-subtracted images with a series of elliptical annuli from the center to the outskirts, with the length of the semi-major axis increasing by 10% in each step. The width of annuli was chosen to increase with radius to suppress noise in the outer regions, where the signal-to-noise is low. The coordinates of the photometric peak in each band were obtained by the DAOPHOT package and were fixed in the fit. The difference in the peak coordinates between the eight bands is less than $0.3''$. We also fixed the sky level in the fit, but kept other parameters, such as ellipticity and position angle, as free parameters. In addition, all foreground and background objects were masked out in order to reduce their contamination. Since our goal was to obtain the radial profile of the SED, it was essential that each elliptical isophotic annulus have the same physical size in all of the eight bands. To achieve this the *r*-band image was used to define isophotic annuli, and these were applied to all the eight bands.

In the SDSS, photometric quantities are usually quoted in the ‘Petrosian’ system (Petrosian 1976). SDSS defines the Petrosian ratio \mathcal{R}_P at a radius r from the center of an object to be the ratio of the local surface brightness averaged over an annulus at r to the mean surface

brightness within r (Blanton et al. 2001; Stoughton et al. 2002):

$$\mathcal{R}_P(r) \equiv \frac{\int_{0.8r}^{1.25r} dr' 2\pi r' I(r') / [\pi(1.25^2 - 0.8^2)r^2]}{\int_0^r dr' 2\pi r' I(r') / [\pi r^2]}, \quad (1)$$

where $I(r)$ is the azimuthally averaged surface brightness profile. The Petrosian radius r_P is defined as the radius at which $\mathcal{R}_P(r_P)$ equals 0.2. The Petrosian flux in any band is then defined to be the flux within two Petrosian radii:

$$F_P \equiv \int_0^{2r_P} 2\pi r' dr' I(r'). \quad (2)$$

The Petrosian half light radius R_{50} is defined as the radius within which 50% of the Petrosian flux is contained.

In our analysis, we cut off the brightness profiles at a radius of $5R_{50}$. At this radius, the surface brightness is about 8% of the g , r , i -skys, and is about 2% of the u , z -skys, and about 0.1-0.3% of the J , H , K_S -skys. The typical values of R_{50} of our sample galaxies are about 7''. Figure 2 shows an example of the surface brightness profiles obtained, in this case for NGC 0430, and Figure 3 shows the corresponding SEDs derived from the fluxes in the eight bands at different radii. To have an overall view of the color gradient for the sample galaxies we are considering, we show in Figure 4 the relative shape of the SED at different radii (in units of R_{50}) in terms of the median values for the 35 sample galaxies. The offset of the SEDs at $0.5R_{50}$ and at $3R_{50}$ is about 0.4 mag from the red end to the blue end. This implies a color gradient in the sample galaxies, in the sense that the stellar light becomes redder toward the central regions. Such gradients will be quantified further in section 4. It is interesting that $\Delta\mu_{median}$ for the i -band shows abnormal behavior at all radii. In the inner region, the i -band surface brightness appears fainter than expected, while in the outer region it is brighter. As we will see in Section 2.2.5 and in the Appendix, this is caused by the so called ‘red-halo’ effect in the i -band.

2.2.3. Calibration

The SDSS magnitudes are quite close to the AB-magnitude system (Oke & Gunn 1983). The zero-point of magnitude for each frame can be obtained directly from the EDR catalogue, and the corrections to the AB system are -0.042, 0.036, 0.015, 0.013, and -0.002 for the u , g , r , i , and z bands respectively (Blanton et al. 2003). The 2MASS zero-point in the Vega magnitude system can be found in the atlas image header. These were converted to AB magnitudes by adding offsets of 0.89, 1.37, and 1.84 for the J , H , and K_S bands respectively (Finlator et al., 2000). Throughout this paper, all magnitudes are in the AB system unless

otherwise stated. In addition, dust extinction by the Milky Way was corrected for each galaxy according to its galactic coordinates as provided by Schlegel, Finkbeiner, & Davis (1998).

2.2.4. Error Estimation

One crucial step in our analysis is to take into account the photometric error in the different wavebands. The observational error in the surface brightness profile consists of the following several components. The first is random error, including the readout noise, the shot noise of the sky background and the shot noise of the galaxy in consideration. At small radii, where the brightness of the galaxy is much higher than the sky background, the noise from the galaxy dominates. On the other hand, at large radii where the brightness of the galaxy is much fainter than the sky background, the noise from the galaxy can be neglected in comparison to the readout noise and the noise of sky background. Here we are concerned mainly with the errors in the outer region, because these errors determine to which radius the observed surface brightness profile can be trusted. In the first row of Table 2, we list the random error in one pixel (expressed in terms of the percentage of sky level), which includes both the readout noise and the noise due to the sky background. Because the radial profile is the average of the flux of all the pixels in the corresponding isophote annulus, the final error introduced by random noise depends on the number of pixels in the annulus. For most of our galaxies, the annulus at $5R_{50}$ contains more than 2,500 pixels in a SDSS image, and more than 400 pixels in a 2MASS image.

The final random errors at $5R_{50}$ are also presented in Table 2. It should be noted that the 2MASS images were produced by averaging 6 frames; the camera pixels were divided

Table 2: The Error Estimation

Source of error (in percentage of the sky level)	<i>u</i>	<i>g</i>	<i>r</i>	<i>i</i>	<i>z</i>	<i>J</i>	<i>H</i>	<i>K_S</i>
Random Noise of each pixel ^a	12.5%	4.0%	2.7%	2.4%	3.0%	0.62%	0.25%	0.20%
Random Noise at $5R_{50}$ ^b	0.25%	0.08%	0.05%	0.05%	0.06%	0.11%	0.04%	0.03%
Background Subtraction	0.54%	0.19%	0.13%	0.17%	0.18%	0.06%	0.02%	0.01%

^a Include both readout noise and random noise of the sky background

^b The isophote annulus at radius of $5R_{50}$ is assumed to contain about 2,500 pixels in a SDSS image and about 400 pixels in a 2MASS image.

into 4 final coadd pixels and the pixel values were smoothed by the Weinberg filter (Jarrett et al. 2000). All these have been taken into consideration in our error estimates.

Another important source of error in the outer part of a galaxy is from background subtraction. This error was estimated in a way similar to that described in Wu et al. (2002) where the deep optical images of the edge-on galaxy NGC 4565 was analyzed. Firstly, all the objects including the target source were masked in the background-subtracted image. Secondly, a series of boxes with a size of $70''$ were used to cover the entire image, where the box size is chosen to be comparable to the typical value of $5R_{50}$ of the sample galaxies, so that they can be used to estimate the large-scale error induced by improper background subtraction and flat-field correction. Finally, the average of the un-masked region in each box is obtained, and the standard deviation of these averages among all the boxes was used as the error of background subtraction. This error is larger than the random noise in the optical bands but lower than the random noise in the near-infrared bands. Note that the background subtraction will not work well if severe airglow variation exists in the near-infrared images (Jarrett et al. 2000).

Absolute calibration errors are also very important in our analysis, because we want to construct the SEDs using the fluxes in different bands. Fortunately, such errors are quite small, about 0.02 mag in all the SDSS and 2MASS bands (Abazajian et al. 2004; Cohen, Wheaton & Megeath 2003).

In conclusion, the total error budget combining all of the errors discussed above is smaller than 0.03 mag in the g -, r -, i -bands, 0.07 mag in the z -band, 0.18 mag in u and about 0.3 mag in J , H , K_S . It should be pointed out here that only the outmost few points in our color profiles have large errors; the total profile of a galaxy is not affected significantly by these uncertainties.

2.2.5. ‘Red Halo’ in the PSF Wings

In addition to the normal photometric corrections discussed above, there was another instrumental effect that affected the surface photometry analysis. Since the SDSS photometry survey uses a thinned CCD for the u , g , r , and i bands, there is an effect referred in the literature as the ‘red halo’ of the PSF wings (e.g. Michard 2002). This effect causes the extended wing of the red-band PSF to be much brighter than that in the blue-band. In the SDSS photometric system, the red halo in the i -band is more apparent than that in the other bands (see Appendix).

Since most of the sample galaxies have sizes of about several arcmins and the red halo

effect appears prominent at about 10 to 50 arcsecs, it is a serious problem in measurements of surface photometry, and will also affect the measured SED and color gradients. As pointed out by Michard (2002), the red halo effect depends on both observational time and the field. To avoid such an effect, we will discard the *i*-band data in the following discussion.

3. COLOR GRADIENTS

Radial surface brightness profiles in eight bands for the 36 sample galaxies were obtained, and a linear least-square method was adopted to fit the derived color profiles. To avoid seeing effects (Young & Currie 1995), an inner radius of $0.4R_{50}$ ($\sim 3''$) was used when fitting. As the data became quite noisy at large radius in the *u*, *J*, *H* and *K_S* bands, the outer radius was cut at $5R_{50}$, which is equivalent to approximately 15 kpc in physical size on average, to ensure the errors lower than 0.1 mag arcsec⁻² in the optical bands (except *u* band).

The color gradients were expressed as $\Delta(m_1 - m_2)/\Delta \log R$ in order to compare with previous results obtained by Peletier et al. (1990) in the optical and by Silva & Elston (1994) in the near-infrared. Figure 5 shows the color gradients for three example galaxies: Ark 402, NGC 0867, and NGC 6359. Four color gradients are presented for each galaxy, from top to bottom in each column. Table 3 presents the gradients of color profiles for all sample galaxies. The last line in Table 3 is the average gradient of each color profile over all sample galaxies. It is clear from Figure 5 and Table 3 that all four color gradients have negative values, indicating that the color becomes bluer from the inner to outer parts in early-type galaxies. This result is in agreement with previous investigations of early-type galaxies (Vader et al. 1988; Franx, Illingworth, & Heckman 1989; Peletier, Valentijn, & Jameson 1990; Peletier et al. 1990; Goudfrooij et al. 1994; Tamura et al. 2000; Tamura & Ohta 2000). Note that the errors quoted in the table include both the fitting error and the errors addressed in previous section. In order to transform the SDSS photometric data to the standard *UBVRI* Vega magnitude system, the formulae of Smith et al. (2002) were used:

$$B = g + 0.47(g - r) + 0.17; \quad (3)$$

$$U - B = 0.75(u - g) - 0.83; \quad (4)$$

$$B - V = 1.02(g - r) + 0.20; \quad (5)$$

$$V - R = 0.59(g - r) + 0.11; \quad (6)$$

Based on the average color gradients given in Table 3, the average color gradients in *U* – *B*, *B* – *V*, and *V* – *R* were -0.13 ± 0.04 , -0.05 ± 0.01 , and -0.03 ± 0.01 mag per dex

in radius respectively. The derived color gradients in $U - R$ and $B - R$ were -0.21 ± 0.04 and -0.08 ± 0.01 mag per dex in radius.

In Table 4 we list the color gradients so obtained along with the results obtained from earlier analyses. Our $U - B$, $B - V$, and $V - R$ color gradients are in very good agreement with those obtained by Idiart, Michard, & de Freitas Pacheco (2002) using 36 early-type galaxies, and by Michard (2000) who reanalyzed 30 ellipticals taken from the literature. The color gradients are also consistent with the $U - R$ and $B - R$ color gradients derived by Peletier et al. (1990) from 39 ellipticals, and by Franx and Illingworth (1990) from 17 ellipticals, and with the $B - R$ color gradients obtained by Tamura & Ohta (2003) from galaxies in Abell 2199 and Abell 2634. All these show that the SDSS images can be used to study the surface photometry of nearby galaxies.

4. AGE AND METALLICITY GRADIENTS

In the preceding section we have seen that significant gradients in optical and near-infrared colors exist for nearby early-type galaxies. In this section these results are used to constrain the age and metallicity of the underlying stellar populations. Because of the age-metallicity degeneracy (Worthey 1994), it is in general difficult to separate these two effects by using only one broad-band color. However since we have observations in seven bands ranging from optical to near-infrared wavelengths with which to probe the underlying SED, an attempt to disentangle the age-metallicity degeneracy can be made using stellar population synthesis models.

In this paper, we use the stellar population synthesis code Gissel01 (Galaxy Isochrone Synthesis Spectral Evolution Library, Bruzual & Charlot 2001) to model our photometry data. This library is a special version that includes the filters of both the SDSS and 2MASS bands, making it possible to directly obtain the magnitudes concerned. This code can be used to produce high-resolution model spectra for a Simple Stellar Population (SSP) at different ages with 6 initial metallicities: 0.0001, 0.0004, 0.004, 0.008, 0.02($\sim Z_{\odot}$), or 0.05. Spectra for other metallicities can be obtained by linear interpolation between these six base spectra. The code assumes the universal initial mass function (IMF) obtained by Kroupa (2001). In most of our discussion, it is assumed that stars in each of the sample galaxies are formed in an instantaneous burst. Once an IMF is chosen, the stellar population is completely determined by its age and metallicity. The sensitivity of our results to this assumption has been tested by considering a model where the stellar ages have a finite spread (see section 4.3).

Table 3: The color gradients of 36 early-type galaxies.

objects	$d(u - g)/d \log R$	$d(g - r)/d \log R$	$d(J - K_S)/d \log R$	$d(g - K_S)/d \log R$
ARK402	-0.12± 0.05	-0.22± 0.01	-0.14± 0.09	-0.74± 0.08
ARK404	-0.22± 0.03	-0.02± 0.01	-0.05± 0.05	-0.10± 0.04
CGCG010-030	-0.15± 0.08	-0.04± 0.01	-0.10± 0.11	-0.26± 0.10
CGCG390-020	0.04± 0.06	-0.06± 0.01	-0.12± 0.06	-0.35± 0.05
GIN060	-0.37± 0.07	-0.13± 0.02	-0.13± 0.09	-0.61± 0.07
IC0590-1	-0.18± 0.05	-0.06± 0.01	-0.11± 0.10	-0.16± 0.08
IC0590-2	-0.23± 0.05	-0.03± 0.03	0.00± 0.08	-0.22± 0.06
IC0891	-0.25± 0.05	-0.04± 0.02	-0.14± 0.09	-0.37± 0.06
IC1517	-0.16± 0.03	-0.01± 0.01	-0.14± 0.04	-0.31± 0.03
IC1639	-0.01± 0.02	-0.02± 0.01	0.10± 0.11	0.03± 0.09
NGC0078b	-0.22± 0.03	-0.08± 0.01	-0.08± 0.07	-0.35± 0.05
NGC0359	-0.29± 0.06	-0.03± 0.01	-0.17± 0.13	-0.34± 0.11
NGC0364	-0.07± 0.07	-0.04± 0.01	-0.01± 0.09	-0.22± 0.07
NGC0426	-0.07± 0.07	-0.05± 0.01	-0.28± 0.06	-0.46± 0.04
NGC0430	-0.23± 0.03	-0.04± 0.01	-0.12± 0.03	-0.25± 0.03
NGC0867	-0.14± 0.07	-0.01± 0.01	0.03± 0.09	-0.15± 0.07
NGC0934	-0.29± 0.03	-0.05± 0.01	-0.25± 0.05	-0.50± 0.03
NGC0936	-0.02± 0.02	-0.02± 0.01	-0.05± 0.03	-0.17± 0.03
NGC3325	-0.10± 0.04	-0.05± 0.01	-0.10± 0.07	-0.16± 0.06
NGC4044	-0.18± 0.05	-0.05± 0.01	-0.01± 0.07	-0.36± 0.05
NGC4493	-0.35± 0.06	-0.07± 0.02	-0.01± 0.15	-0.36± 0.12
NGC5865	-0.32± 0.06	-0.07± 0.01	-0.10± 0.11	-0.47± 0.09
NGC5869	-0.06± 0.04	-0.04± 0.01	-0.09± 0.07	-0.19± 0.06
NGC6319	-0.09± 0.05	0.04± 0.02	-0.22± 0.07	-0.52± 0.05
NGC6359	-0.26± 0.03	-0.08± 0.01	-0.16± 0.03	-0.35± 0.02
NGC6382	-0.14± 0.05	-0.10± 0.01	-0.15± 0.07	-0.26± 0.05
NGC6391	-0.26± 0.04	-0.10± 0.01	-0.04± 0.05	-0.24± 0.04
NGC7684	-0.13± 0.02	-0.06± 0.01	0.05± 0.07	-0.06± 0.06
UGC00588	-0.18± 0.06	-0.04± 0.01	-0.11± 0.08	-0.33± 0.06
UGC00599	-0.20± 0.06	-0.05± 0.01	-0.16± 0.08	-0.30± 0.06
UGC00797	-0.36± 0.09	-0.02± 0.01	-0.05± 0.13	-0.22± 0.10
UGC01072	-0.15± 0.03	-0.03± 0.01	-0.05± 0.07	-0.04± 0.05
UGC05515	-0.25± 0.07	-0.06± 0.01	0.10± 0.12	-0.19± 0.09
UGC06435	-0.16± 0.05	-0.11± 0.01	-0.12± 0.08	-0.28± 0.06
UGC07177	-0.02± 0.12	0.01± 0.02	0.02± 0.20	-0.16± 0.15
UGC07813	-0.22± 0.05	-0.07± 0.01	-0.16± 0.08	-0.34± 0.07
Average	-0.18± 0.06	-0.05± 0.01	-0.09± 0.08	-0.29± 0.07

4.1. Color-Color Diagrams

It is useful to first look at the color-color plots to see how the combination of optical and near infrared data can help to break the age-metallicity degeneracy. As an example, Figure 6 shows such a plot for NGC 4044. Colors of this galaxy at different radii are plotted as different symbols. The grids are based on the SSP model. The dashed lines represent loci of constant metallicities, while the dotted lines are the loci of constant ages. From the figure, we can clearly see that (1) all of the colors vary with radius, indicating color gradients; (2) optical colors alone are not effective in breaking the age-metallicity degeneracy (the constant-age loci are almost parallel to the constant-metallicity loci in the optical color-color plots); (3) the use of near-infrared band colors can help greatly to break the age-metallicity degeneracy (the constant-age loci are no longer parallel to the constant-metallicity loci), though the errors in the near-infrared colors given by the 2MASS are quite large. However, although color-color plots are useful visual presentations, they are not the most effective way to quantify the observational results. On the other hand, fitting the SEDs represented by all of the observed colors can provide quantitative constraints on the age and metallicity of the underlying stellar population. Therefore, in the follows we will only use direct fitting of the SEDs to quantify the age and metallicity gradients.

4.2. Fitting the Observed SEDs with Spectral Synthesis Model

Standard χ^2 minimization was used to fit the observed SEDs with the synthesized spectra at different ages and metallicities. Because both optical and near-infrared data were used, the approach can put rigorous constraints on either metallicity or age, if the other is kept fixed. To demonstrate this, we generated test SEDs directly from the spectral synthesis model with given metallicities and ages. Each model magnitude was assigned an observational error σ_{obs} that is equal to the median observational error at R_{50} (defined in

Table 4: Comparison of color gradients.

	$(U - B)$	$(B - V)$	$(V - R)$	$(U - R)$	$(B - R)$
This work	-0.13 ± 0.04	-0.05 ± 0.01	-0.03 ± 0.01	-0.21 ± 0.04	-0.08 ± 0.01
Idiart(2002)	-0.13 ± 0.04	-0.07 ± 0.02	-0.02 ± 0.01		
Michard(2000)	-0.15 ± 0.05	-0.06 ± 0.03	-0.02 ± 0.03		
Peletier(1990)				-0.20	-0.09
Franx(1990)				-0.23 ± 0.03	-0.07 ± 0.01
Tamura(2003)					-0.09 ± 0.04

Section 2.2.2). In addition, an uncertainty from the model itself was included in the error budget, σ_{mod} . Charlot, Worthey, & Bressan (1996) estimated this uncertainty by comparing the colors obtained from different stellar evolutionary tracks and spectral libraries. To take this into account, a model error of 0.05 mag was included in all of our analysis. The combined error for each band was assumed to be the sum in quadrature,

$$\sigma^2 = \sigma_{\text{obs}}^2 + \sigma_{\text{mod}}^2. \quad (7)$$

Tests using other values of σ_{mod} in the range from 0.03 to 0.07 mag showed that such a change does not affect our results significantly.

Figure 7 shows contours of $\Delta\chi^2 \equiv \chi^2 - \chi^2_{\text{min}}$ in the age-metallicity plane for the test SEDs obtained by using different combinations of broad-band photometry. The crosses indicate the input values for the age and metallicity of the stellar population. From Figure 7(a), it is clear that using the combined SDSS and 2MASS data, the age and metallicity is constrained within a very narrow strip. If either the age or the metallicity is chosen as a fixed value, the other parameter can be determined to within 10%. On the other hand, the age and metallicity are still degenerate in some extent even though we include near infrared bands. Comparing Figure 7(a) and (b), one can see that the exclusion of the *i*-band data does not have a significant effect. However, if three or more bands are removed, the error bars become substantially larger (cf. Figure 7 [c] and [d]). Thus, if optical to near-infrared SEDs are used, much more accurate parameters can be obtained than when only one or two colors are available. This figure also shows that the 2MASS data can significantly reduce the size of contours, even though errors of the 2MASS data are larger. In conclusion, more photometric bands and the extension of the wavelength coverage are both important for determining the age and metallicity in galaxies.

Because the age-metallicity degeneracy still exist, it is quite difficult to estimate the age and metallicity simultaneously for individual galaxies. However, for statistical purpose, we worked out the best-fit of age and metallicity for the sample galaxies, which are are widely spread, from age of 3 to 9 Gyrs and metallicity of 1 to $2 Z_{\odot}$. These results are consistent with those of Trager et al. (2000).

4.3. The Radial Gradients of Age and Metallicity

To obtain the age and metallicity gradients from the observed color gradients, it was assumed that the SED for each projected annulus can be described by a single stellar population, and χ^2 fitting as described above was used to determine ages and metallicities. Firstly, the assumption was made that the observed color gradients are purely due to either age or

metallicity by fixing one of the two parameters (metallicity or age) at the best-fit value for R_{50} . Secondly, the gradients were modelled by treating both the age and metallicity as free parameters.

Figure 8 shows the results of such analysis for NGC 4044. Panel (a) shows the contour of $\Delta\chi^2$ in age-metallicity space for the annulus at R_{50} , while panel (b) shows the observed SED for this annulus together with the best model fit. It is clear from Figure 8 that the observed SED is well reproduced by a single burst model, and the $\Delta\chi^2$ contour map looks similar to those for the test galaxies shown in Figure 7. Panel (c) shows the best-fit metallicity as a function of radius, where the stellar age is fixed to be 9.1 Gyr (the best fit age at R_{50}) across the entire galaxy. A metallicity gradient is clearly seen here. The two vertical dashed lines indicate the radii $0.4R_{50}$ and $5.0R_{50}$, within which the observational SEDs are not seriously affected by seeing and have a sufficiently high signal-to-noise ratio. The gradient was fitted by a linear function of $\log(R)$ within this radius range. Panel (d) shows the age profile where the metallicity is assumed to be a constant across the galaxy.

From panel (c) and (d) of Figure 8, one can see that the radial gradients of either metallicity or age can be well described as a linear relationship in logarithmic space. The two slopes

$$g_Z \equiv \frac{d \log Z_{\text{met}}}{d \log R} \quad \text{and} \quad g_A \equiv \frac{d \log \text{Age}}{d \log R} \quad (8)$$

were thus defined in order to characterize the metallicity and age gradients respectively. Fitting the observational data for each galaxy assuming either g_A or g_Z is zero, the distribution of g_Z or g_A was obtained, see Figure 9. All galaxies except NGC 6319 were well fitted by this method. Because the SED of NGC 6319 could not be fitted by any simple synthesis model, this galaxy was excluded from our analysis. The median values for the remaining 35 galaxies were $g_Z \sim -0.22$ and $g_A \sim -0.31$ respectively.

In order to constrain the metallicity and age gradients simultaneously, it was assumed that for each galaxy these gradients can be described by linear relations in log-log space with slopes g_Z and g_A . Here again, the quantities at the radius R_{50} of a galaxy were used as the zero point of the relations for the galaxy. For given values of g_Z and g_A , a model galaxy was constructed with stellar populations specified by the age and metallicity gradients. The values of g_Z and g_A were then determined for each galaxy by matching the predicted SEDs at different radii with the observed values. In addition, χ^2 minimization was used to obtain the best-fit values of g_A and g_Z , and data points in the radius range from $0.4R_{50}$ to $5.0R_{50}$ were used in the fit. Figure 10 shows the contour maps of $\Delta\chi^2$ in g_A - g_Z space for two example galaxies. It can be seen that the constraints on g_Z and g_A are not equally rigorous for different galaxies.

Figure 11 shows the best-fit values of g_Z and g_A for the 35 sample galaxies. In order to obtain statistical constraints on g_A and g_Z for the entire sample, the $\Delta\chi^2$ contours for each galaxy were used to obtain a galaxy-possibility distribution in $g_Z - g_A$ space. Then, all galaxies were summed to have a possibility distribution for the sample, $P(g_Z, g_A)$. The contours of this distribution function are plotted in Figure 11. Figure 12 shows the projections of this distribution function along the two axes. Each can be fitted reasonably well by a Gaussian profile. Based on this we obtain $g_Z = -0.25 \pm 0.03$, $\sigma_{g_Z} = 0.19 \pm 0.03$, and $g_A = 0.02 \pm 0.04$, $\sigma_{g_A} = 0.25 \pm 0.03$. Note that the contours shown in Figure 11 are elongated along the line of age-metallicity degeneracy, and so it is likely that the dispersions in g_A and g_Z are dominated by this degeneracy. Since the best-fit value for g_A is close to zero, the result is consistent with the hypothesis that all the observed gradients in the SEDs of these early-type galaxies are due to metallicity variations. Indeed, the median value of g_Z obtained here is consistent with that obtained above with the assumption of $g_A \equiv 0$. The result is inconsistent with the hypothesis that these gradients are due to age variations.

The above results are based on the assumption that stars in an elliptical galaxy were formed in an instantaneous burst with zero age spread. An important question is how sensitive these results are to this assumption. To investigate this, models in which the star formation rate in a galaxy changes with time as $\text{SFR} \propto \exp(-t/\tau)$ were considered, where τ is a constant characterizing the spread in the ages of the stellar population. As an illustration, we considered three cases where τ is equal to 0.5, 1.0, and 2.0 Gyrs respectively. Note that the SSP considered above corresponds to $\tau = 0$. In such models, the two parameters that characterize the stellar population are the initial metallicity and starting time for star formation. The same procedure as for the SSP case was used to determine the median and dispersion for g_Z and g_A . Results are listed in Table 5, along with the results for the SSP ($\tau = 0$) case. Clearly, our conclusions about the age and metallicity gradients are quite insensitive to the assumption of the spread of stellar age. Calculations using still larger values of τ have shown that significant differences occur only when τ becomes larger than 8 Gyr.

Table 5: Metallicity gradients, age gradients, and their dispersions obtained with different star formation time scales.

	g_Z	σ_{g_Z}	g_A	σ_{g_A}
SSP	-0.25 ± 0.03	0.19 ± 0.03	0.02 ± 0.04	0.25 ± 0.03
$\tau = 0.5Gyr$	-0.24 ± 0.03	0.21 ± 0.03	0.04 ± 0.04	0.21 ± 0.03
$\tau = 1.0Gyr$	-0.26 ± 0.04	0.24 ± 0.03	0.05 ± 0.03	0.19 ± 0.02
$\tau = 2.0Gyr$	-0.26 ± 0.04	0.26 ± 0.04	0.02 ± 0.03	0.17 ± 0.02

5. DISCUSSION

5.1. The Effect of Dust

It must be kept in mind that the results presented above have neglected dust absorption in the host galaxies. Since dust obscuration reddens stellar light, the existence of dust changes the color of a galaxy, and can mimic a color gradient if the distribution of dust has a gradient. Although many elliptical galaxies contain significant amounts of interstellar matter (Roberts et al. 1991), most is in the form of hot X-ray gas, and only a small fraction (about $10^7 M_\odot$) is in the form of dust (Kormendy & Djorgovski 1989; Forbes 1991; Goudfrooij 1994; Wise & Silva 1996). van Dokkum & Franx (1995) used HST images to study the dust properties of a sample of 64 early-type galaxies. They found that 48% of them show dust absorption, but that dust absorption is highly concentrated to the nuclear regions. The sizes of these absorption regions at the major axes are much smaller than 1 kpc for almost all their sample galaxies (only 3 have a dust distribution size of 2 kpc). In recent observations of 6 early type galaxies in infrared PAH bands by the Spitzer Space Telescope (Pahre et al. 2004) 3 of these 6 early-type galaxies exhibit dust features and the dust distribution have a size of about 1 to 3 kpc.

However, dust distribution in early type galaxies is still poorly understood; only simple models are available to investigate possible effect of the dust extinction on color gradients. Here we follow Wise & Silva (1996) and consider three simple models for the dust distribution. The most likely case is that of a concentrated dust distribution, which is suggested by current observations. If dust distribution has a spatial density distribution of $\rho_d(r) \sim r^{-3}$ or is even more concentrated, then dust absorption is only significant in the very central region of the galaxy (~ 1 kpc; see Fig. 8 in Wise & Silva 1996). In this case, dust extinction will not have any effect on our results, since we have excluded the central region of a galaxy (within $0.4R_{50}$, ~ 1.4 kpc on average) in our analysis. The second case is a flat density distribution of dust $\rho_d(r) \sim r^0$. In this case, dust absorption is almost the same over the whole body of a galaxy, and it will not produce any radial gradients in colors (or in the SEDs). A third case is a distribution between these two extreme cases. According to Wise & Silva's analysis, if the dust is distributed as $\rho_d(r) \sim r^{-1}$, it will cause a linear color gradient with $\log R$, which can be confused with true metallicity and/or age gradients. To be conservative, we consider here the effect of dust extinction assuming such a distribution.

Following Charlot & Fall (2000), we assume a power-law form for the dust absorption curve: $\tau_\lambda = \tau_V(\lambda/5500\text{\AA})^{-0.7}$. The absorption by dust can then be parameterized with a single parameter τ_V , which is the effective optical depth at a wavelength of 5500\AA . Another assumption is that $\tau_V(R)$ decreases linearly with $\log R$, and approaches *zero* in the outer

region (in practice, we set $\tau_V(10R_{50}) \equiv 0$). This absorption model can also be derived from Wise & Silva's (1996) calculations (see the dotted line in their Fig.8). Thus only one additional free parameter, $\tau_V(R_{50})$, is needed to describe the absorption of such a diffuse distribution of dust as a function of radius R .

The SSP fitting procedure was then carried out by convolving the absorption curves at different radii with the given values of $\tau_V(R_{50})$, and the effects on age and metallicity gradients recorded. We have done several tests with different values of $\tau_V(R_{50})$, and the results are summarized in Table 6. Compared with the dust-free case $\tau_V(R_{50}) = 0$, it is clear that the existence of a diffuse dust distribution can indeed cause a radial color gradient and thereby reduce the degree of metallicity gradients. However, it does not change the average value of the age gradients. If the total amount of diffusing dust is large enough so that $\tau_V(R_{50}) \sim 0.4$, the different levels of absorption at different radii can explain all the observed color gradients in our sample. From Wise & Silva's calculation, about $10^6 M_\odot$ of diffuse dust is needed to produce the required $\tau_V(R_{50}) \sim 0.4$.

The dust model we have used is likely too simple to describe the dust distribution in galaxies realistically. More precise description of the dust distribution in early-type galaxies may be possible with the future observations, such that from the Spitzer Space Telescope. In summary, the presence of diffuse dust distribution can mimic the color gradients we have observed, and the metallicity gradients we obtained ($g_Z \sim -0.25$) is only robust if the amount of dust in the diffuse distribution is negligible.

5.2. Theoretical Implications

Simulations of the formation of elliptical galaxies through monolithic collapse (e.g. Carlberg 1984) have shown that the metallicity gradients predicted by this model are quite steep, with g_Z at least as steep as -0.5. This is clearly in conflict with our average result of $g_Z \sim -0.25$. On the other hand, recent simulations of Kobayashi (2004) showed that metal-

Table 6: Metallicity gradients, age gradients, and their dispersions obtained with different dust absorption levels.

$\tau_V(R_{50})$	g_Z	σ_{g_Z}	g_A	σ_{g_A}
0.0	-0.25 ± 0.03	0.19 ± 0.03	0.02 ± 0.04	0.25 ± 0.03
0.1	-0.19 ± 0.04	0.22 ± 0.03	0.02 ± 0.04	0.23 ± 0.03
0.2	-0.13 ± 0.04	0.22 ± 0.03	0.00 ± 0.04	0.23 ± 0.03
0.4	-0.02 ± 0.04	0.21 ± 0.03	0.00 ± 0.03	0.18 ± 0.03

licity gradients can be significantly flattened by strong mergers. They showed that galaxies formed through major mergers have $\Delta \log Z / \Delta \log R \sim -0.22$ and none of them have a gradient steeper than -0.35 , while galaxies formed through minor mergers or monolithic collapse are quite similar, with metallicity gradients of approximately -0.3 . Our average metallicity gradient is between -0.22 and -0.30 , but individual gradients span a wide range from -0.6 to above zero. Since Kobayashi used a similar radius range as ours to measure gradients, we can compare our observational results directly with her simulations. To proceed, we adopt a metallicity gradient of -0.26 to separate galaxies into two subsamples. According to Kobayashi’s results, the subsample with metallicity gradients shallower than -0.26 would be galaxies dominated by a major merger, while those with steeper metallicity gradients are the ones whose formation would be dominated by minor mergers or monolithic collapse. In Figure 13 we plot the absolute magnitude (M_B) distribution for these two subsamples of galaxies. Although the average M_B is similar for the two subsamples (about $M_B \sim -20.5$), the two distributions are different. Most of the galaxies in the subsample with $g_Z < -0.26$ (i.e. the one with steeper gradient) are fainter. Since nearly half of our galaxies are S0 galaxies which have luminosities lower than elliptical galaxies, it is possible that the subsample with lower gradients is in fact dominated by S0 galaxies. Unfortunately, the sample is too small to allow us to probe the detailed dependence on morphological type. The subsample with lower gradients also includes the three brightest galaxies in the whole sample (UGC05515, UGC00797 and NGC 5865). It is interesting that UGC00797 is a cD galaxy and the other two also look like cD galaxies from their environment and radial profiles. If merger plays an important role in determining the metallicity gradient, as discussed above, this result would mean that cD-like galaxies and faint ellipticals form through many minor mergers and/or monolithic collapse. Our current sample is still too small to make a strong statement, but this question can be addressed with large samples to be constructed from the SDSS and the 2MASS.

Another interesting result is that we obtain a quite large scatter in g_Z , ~ 0.2 . This cannot be explained by the uncertainties in measurement or fitting alone, which are approximately an order of magnitude lower. Thus, such scatter must be intrinsic. In this study we have not separated galaxies according to morphology (e.g. lenticulars versus ellipticals, normal ellipticals versus cDs) and environment, and the large scatter may be partly due to morphology and environment dependence. Our result is also consistent with the simulation of Kobayashi (2004), who obtained similar scatter among all the galaxies in her simulation.

The average value of the age gradient we found, $g_A \sim 0$, suggests that stars over a wide range of radius in early-type galaxies (0.4 to $5.0 R_{50}$ as probed in this paper), have approximately the same age. This is consistent with the monolithic collapse formation scenario, where the bulk of stars in a galaxy formed in a single burst, or with similar star

formation history over the whole galaxy. However, the lack of a significant age gradient does not contradict with the hierarchical formation scenario, if early-type galaxies formed their stars early in their progenitors.

6. SUMMARY

In this paper we have analyzed the optical and near-infrared surface photometry of a sample of 36 nearby early-type galaxies based on broad-band images obtained from SDSS and 2MASS. The optical and near-infrared color gradients of each galaxy have been derived and modelled in terms of metallicity and age gradients in their underlying stellar populations. Our main results are summarized as follows:

1. Almost all galaxies show shallow color gradients in the five SDSS bands and the three 2MASS bands. The measured average color gradients in $U - R$, $B - R$, and $J - K_S$ are -0.21 , -0.08 , and -0.09 respectively, in agreement with previous results.
2. For the first time, SEDs from optical to near-infrared wavelengths have been used to analyze the stellar population distribution of early-type galaxies. Both tests and results have proved the strength of combining SDSS and 2MASS data in the study of stellar populations.
3. Fitting both the age and metallicity simultaneously with stellar population synthesis models, and using $g_Z = d \log Z / d \log R$ and $g_A = d \log \text{Age} / d \log R$ to represent the metallicity and age gradients, a median value of $g_Z = -0.25 \pm 0.03$ was found for the metallicity gradient, with a dispersion of $\sigma_{g_Z} = 0.19 \pm 0.02$. Corresponding values for the age gradient are $g_A = 0.02 \pm 0.04$ and $\sigma_{g_A} = 0.25 \pm 0.03$. These results are in good agreement with other observational results and with the expectations of current theories of galaxy formation.
4. A diffuse distribution of dust [$\rho_d(r) \sim r^{-1}$] could produce a linear color gradient with $\log R$, but it will not change the result that the average age gradient is ~ 0 . If any diffusely distributed dust exists, it would decrease metallicity gradients, which would further support the hypothesis that major mergers play an important role in the formation of the early-type galaxies.

Given the amount of new data now available from the 2MASS and the current SDSS (DR2), and data soon to be available from the SDSS and the Spitzer Space Telescope in the near future, it will be possible to compile a sample of several hundred large early-type

galaxies to carry out the same analysis as presented in this paper. Our results presented here suggest that with such a sample, it will be possible to study the age-metallicity gradients of early-type galaxies in unprecedented detail.

7. ACKNOWLEDGEMENTS

The authors thank Ivan Baldry, Stephen Charlot, Daniel Thomas, Claudia Maraston, Shude Mao, Jiasheng Huang, Peter Williams, Zhong Wang, J. Mo, Shiyan Shen, Zhenlong Zou, Jingyao Hu, Hongjun Su, Xu Zhou and Jianyan Wei for their helpful advice and discussions. We also thank an anonymous referee for his/her helpful suggestions. This project is supported by NSF of China No.10273012, No.10273016, No.10333060, No.10473013 and NKBSRF G19990754.

Funding for the creation and distribution of the SDSS Archive has been provided by the Alfred P. Sloan Foundation, the Participating Institutions, the National Aeronautics and Space Administration, the National Science Foundation, the U.S. Department of Energy, the Japanese Monbukagakusho, and the Max Planck Society. The SDSS Web site is <http://www.sdss.org/>. The SDSS is managed by the Astrophysical Research Consortium (ARC) for the Participating Institutions. The Participating Institutions are The University of Chicago, Fermilab, the Institute for Advanced Study, the Japan Participation Group, The Johns Hopkins University, Los Alamos National Laboratory, the Max-Planck-Institute for Astronomy (MPIA), the Max-Planck-Institute for Astrophysics (MPA), New Mexico State University, Princeton University, the United States Naval Observatory, and the University of Washington.

This publication makes use of data products from the Two Micron All Sky Survey, which is a joint project of the University of Massachusetts and the Infrared Processing and Analysis Centre/California Institute of Technology, funded by the Aeronautics and Space Administration and the National Science Foundation.

A. RED HALO OF PSF WINGS OF SDSS IMAGES

Michard (2002) studied the PSFs of thinned CCDs in different bands, concluding that atmospheric seeing dominates the central range of the PSF, and that the effects of seeing disappear at around $15''$. However, in the outer regions, the wing of the PSF is controlled by both instrumental and atmospheric scattering. The extended wing of the red-band PSF is much brighter than that of the blue band in thinned CCDs. This is referred to as the ‘red

halo' effect (Michard 2002; Idiart, Michard, & de Freitas Pacheco 2002).

The SDSS project employs 30 Tektronix/SITe 2048×2048 CCDs in a 5 by 6 array for the five bands, with 6 unthinned frontside CCDs for the z -band, and 24 thinned backside CCDs for the other four bands. To explore the outer PSF wings in these five bands, isolated unsaturated and saturated stars in different EDR fields were selected. All of these fields were sky subtracted and the median intensity was measured in concentric circles around each star to avoid the effect of asymmetric features of saturated stars, and of foreground and background objects. The profiles of all stars for each band were re-scaled to the same size and combined. The mean PSF profiles in the five bands were then obtained.

Figure 14 shows the radial profiles of the mean PSFs in the five bands. The red halo problem is clearly apparent. The i -band profile is quite different from the other four bands at radii starting from about $6''$, consistent with the results of Michard (2002). Thus the red halo effect is expected to affect the surface brightness profiles of galaxies at radii larger than $\sim 10''$. The PSF profiles in the g , r , and z bands agree very well with each other. Although the z -band is much redder than the i -band, there is no red halo problem because unthinned CCDs are used. This confirms that the red halo effect only appears in thinned CCDs. The u -band PSF is slightly higher than those of the g , r , and z bands, but much lower than that of the i -band. In this paper we neglect this small difference between the u -band and the g , r , and z bands.

REFERENCES

Abazajian, K., et al. 2004., AJ, 128, 502

Baum, W.A., Thomsen, B., & Morgan, B.L. 1986, ApJ, 301, 83

Bertin, E., & Arnouts, S. 1996, A&AS, 117, 393

Blanton, M.R., et al. 2001, ApJ, 121,2358

Blanton, M.R., et al. 2003, ApJ, 594, 186

Boroson, T.A., Thompson, I.B., & Shectman, S.A. 1983, AJ, 88,1707

Cardiel, N., Gorgas, J., Sánchez-Blázquez, P., Cenarro, A.J., Pedraz, S., Bruzual, G., & Klement, J. 2003, A&A, 409, 511

Carlberg, R.G. 1984, ApJ, 286, 416

Carollo, C.M., Danziger, I.J., & Buson, L. 1993, MNRAS, 265, 553

Charlot, S., & Fall, S. 2000, *ApJ*, 539, 718

Charlot, S., Worthey, G., & Bressan, A. 1996, *ApJ*, 457, 625

Cohen, J.G. 1986, *AJ*, 92, 1039

Cohen, M., Wheaton, W.A., & Megeath, S.T. 2003, *AJ*, 126, 1090

Cutri, R.M., et al. 2000, Explanatory Supplement to the 2MASS Second Incremental Data Release (Pasadena: Caltech)

de Jong, R.S. 1996, *A&A*, 313, 377

de Vaucouleurs, G. 1961, *ApJS*, 5, 233

de Vaucouleurs, G., de Vaucouleurs, A., Corwin, H.G., Buta, R.J., Paturel, G., & Fouque, P. 1991, Third Reference Catalogue of Bright Galaxies (RC3), Springer-Verlag: New York

Davies, R.L., Sadler, E.M., & Peletier, R.F. 1993, *MNRAS*, 262, 650

Davis, L.E., Cawson, M., Davies, R.L., & Illingworth, G. 1985, *AJ*, 90, 169

Finlator, K., et al. 2000, *AJ*, 120, 2615

Forbes, D.A. 1991, *MNRAS*, 249, 779

Franx, M., Illingworth, G., & Heckman, T. 1989, *AJ*, 98, 538

Franx, M., & Illingworth, G. 1990, *ApJ*, 359, L41

Goudfrooij, P., Hansen, L., Jorgensen, H.E., Norgaard-Nielsen, H.U., de Jong, T., & van den Hoek, L.B. 1994, *A&AS*, 104, 179

Henry, R.B.C., & Worthey, G. 1999, *PASP*, 111, 919

Hinkley, S., & Im, M. 2001, *ApJ*, 560, L41

Idiart, T.P., Michard, R., & de Freitas Pacheco, J.A. 2002, *A&A*, 383, 30

Idiart, T.P., Michard, R., & de Freitas Pacheco, J.A. 2003, *A&A*, 398, 949

Jarrett, T.H., Chester, T., Cutri, R., Schneider, S.E., & Huchra, J.P. 2003, *AJ*, 125, 525

Jarrett, T.H., Chester, T., Cutri, R., Schneider, S.E., Skrutskie, M., & Huchra, J.P. 2000, *AJ*, 119, 2498

Kobayashi, C. 2004, MNRAS, 347, 740

Kormendy, J., & Djorgovski, S. 1989, ARA&A, 27, 235

Kroupa, P. 2001, MNRAS, 322, 231

Larson, R.B. 1974, MNRAS, 166, 585

MacArthur, L.A., Courteau, S., Bell, E., & Holtzman, J.A. 2004, ApJS, 152, 175

Mehlert, D., Saglia, R.P., Bender, R., & Wegner, G. 2000, A&AS, 141, 449

Mehlert, D., Thomas, D., Saglia, R.P., Bender, R., & Wegner, G. 2003, A&A, 407, 423

Michard, R. 1999, A&AS, 137, 245

Michard, R. 2000, A&A, 360, 85

Michard, R. 2002, A&A, 384, 763

Nakamura, O., et al. 2003, AJ, 125, 1682

Oke, J.B., & Gunn, J.E. 1983, ApJ, 266, 713

Pahre, M.A., Ashby, M.L.N., Fazio, G.G., & Willner, S.P. 2004, ApJS, 154, 229

Peletier, R.F., Davies, R.L., Illingworth, G.D., Davis, L.E., & Cawson, M. 1990, AJ, 100, 1091

Peletier, R.F., Valentijn, E.A., & Jameson, R.F. 1990, A&A, 233, 62

Petrosian, V. 1976, ApJ, 209, L1

Roberts, M.S., Hogg, D.E., Bregman, J.N., Forman, W.R., & Jones, C. 1991, ApJS, 75, 751

Saglia, R.P., Maraston, C., Gregg, L., Bender, R., & Ziegler, B. 2000, A&A, 360, 911

Schlegel, D.J., Finkbeiner, D.P., & Davis, M. 1998, ApJ, 500, 525

Scuderi, M. 2001 AJ, 121, 2413

Silva, D.R., & Elston, R. 1994, ApJ, 428, 511

Smith, J.A., et al. 2002, AJ, 123, 2121

Stoughton, C., et al. 2002, AJ, 123, 485

Tamura, N., & Ohta, K. 2000, AJ, 120, 533

Tamura, N., Kobayashi, C., Arimoto, N., Kodama, T., & Ohta, K. 2000, AJ, 119, 2134

Tamura, N., & Ohta, K. 2003, AJ, 126, 596

Trager, S.C., Faber, S.M., Worthey, G., & González, J.J. 2000, AJ, 119, 1645

Vader, J.P., Vigroux, L., Lachieze-Rey, M., & Souviron, J. 1988, A&A, 203, 217

van Dokkum, P.G., & Franx, M. 1995, AJ, 110, 2027

White, S.D.M. 1980, MNRAS, 191, 1

Wise, M.W., & Silva, D.R. 1996, ApJ, 461, 155

Worthey, G. 1994, ApJS, 95, 107

Wu, H., et al. 2002, AJ, 123, 1364

Young, C.K., & Currie, M.J. 1995, MNRAS, 273, 1141

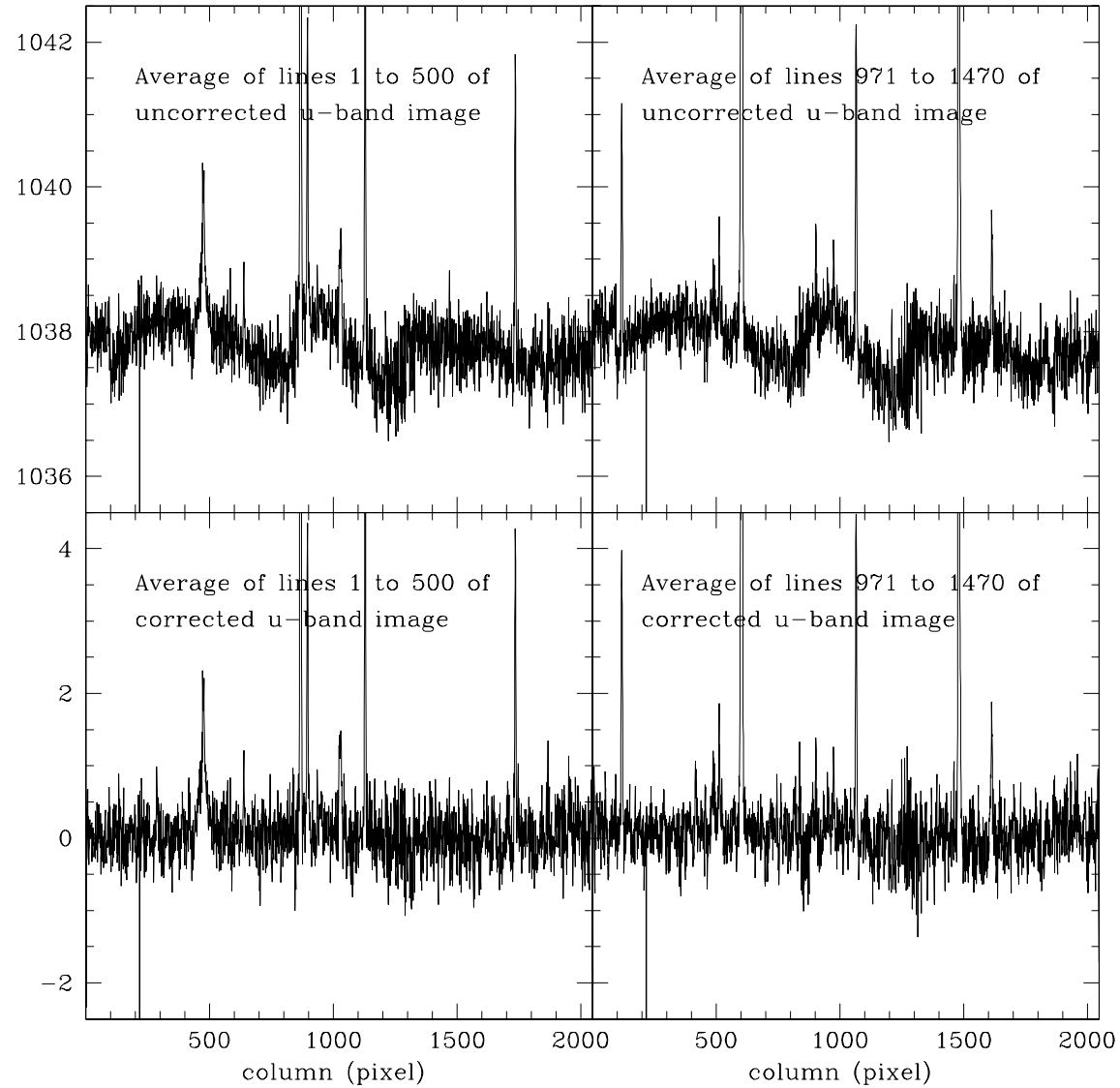


Fig. 1.— The two upper panels show the averages of 500 lines in the upper and lower parts of one SDSS imaging frame. The fluctuation patterns are similar suggesting they are spurious features at a level of $\sim 1 - 2$ ADU. The two lower panels show the average after correction. Note that the spurious features have been successfully removed by our method.

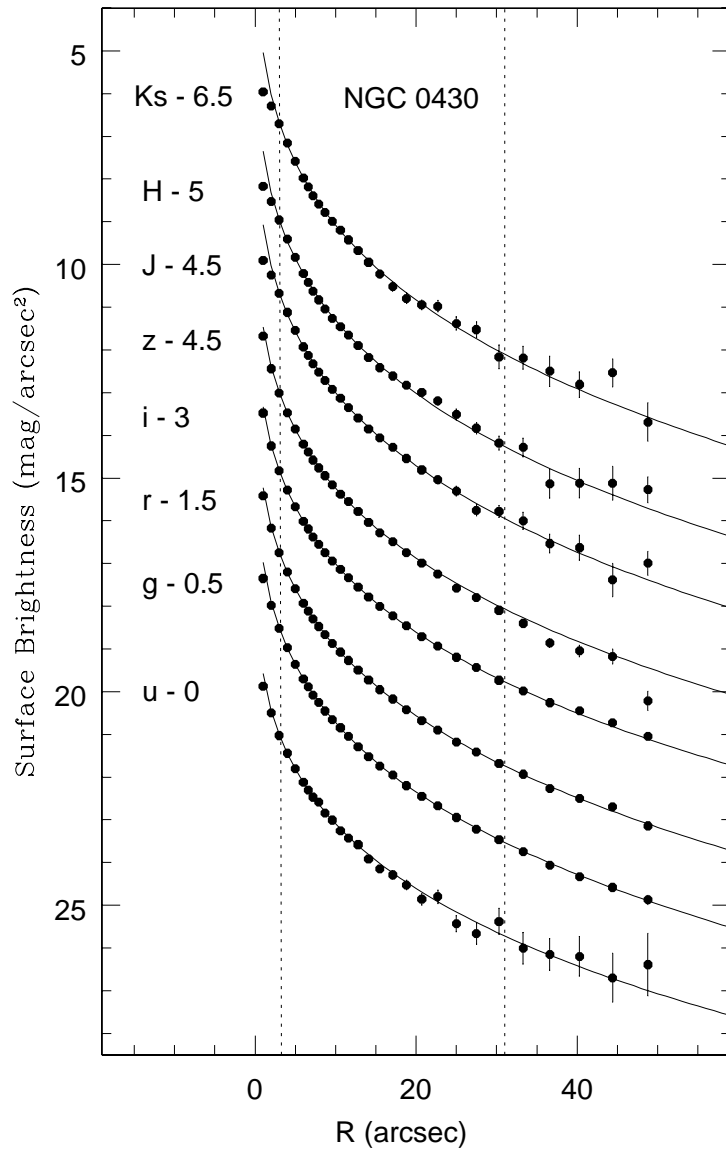


Fig. 2.— The measured surface brightness of NGC 0430 as a function of radius in the optical and near-infrared bands. The profiles are shifted for clarity. Error bars, defined in the text, are also plotted for each measured point. The vertical dotted lines mark the region of $0.4R_{50}$ and $5R_{50}$ used for analysis. The curves are best-fit de Vaucouleurs profiles.

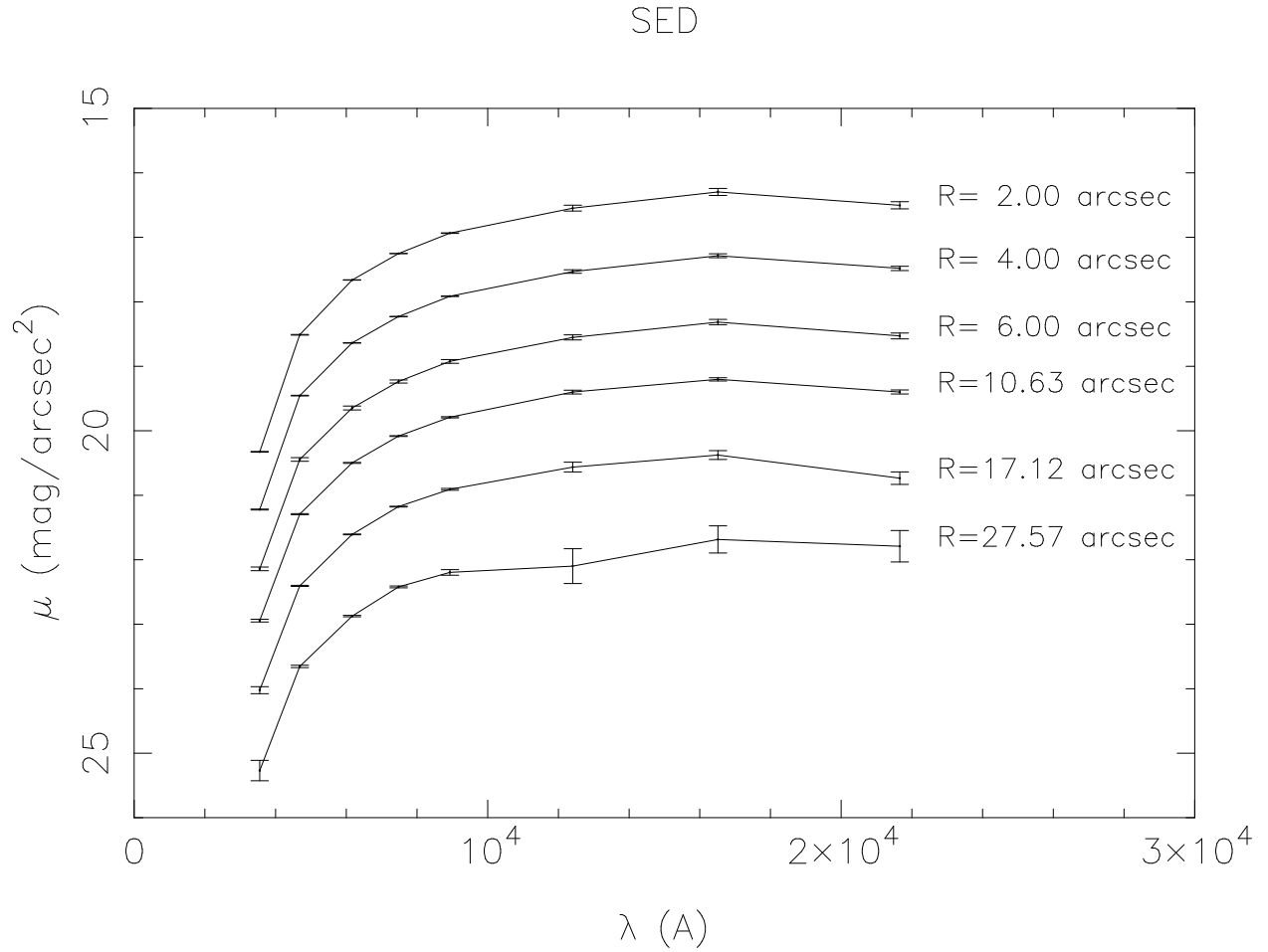


Fig. 3.— SEDs of NGC 0430 at different radii as represented by the surface brightness in eight bands. The value of R_{50} for this galaxy is about $6.0''$ in the r -band.

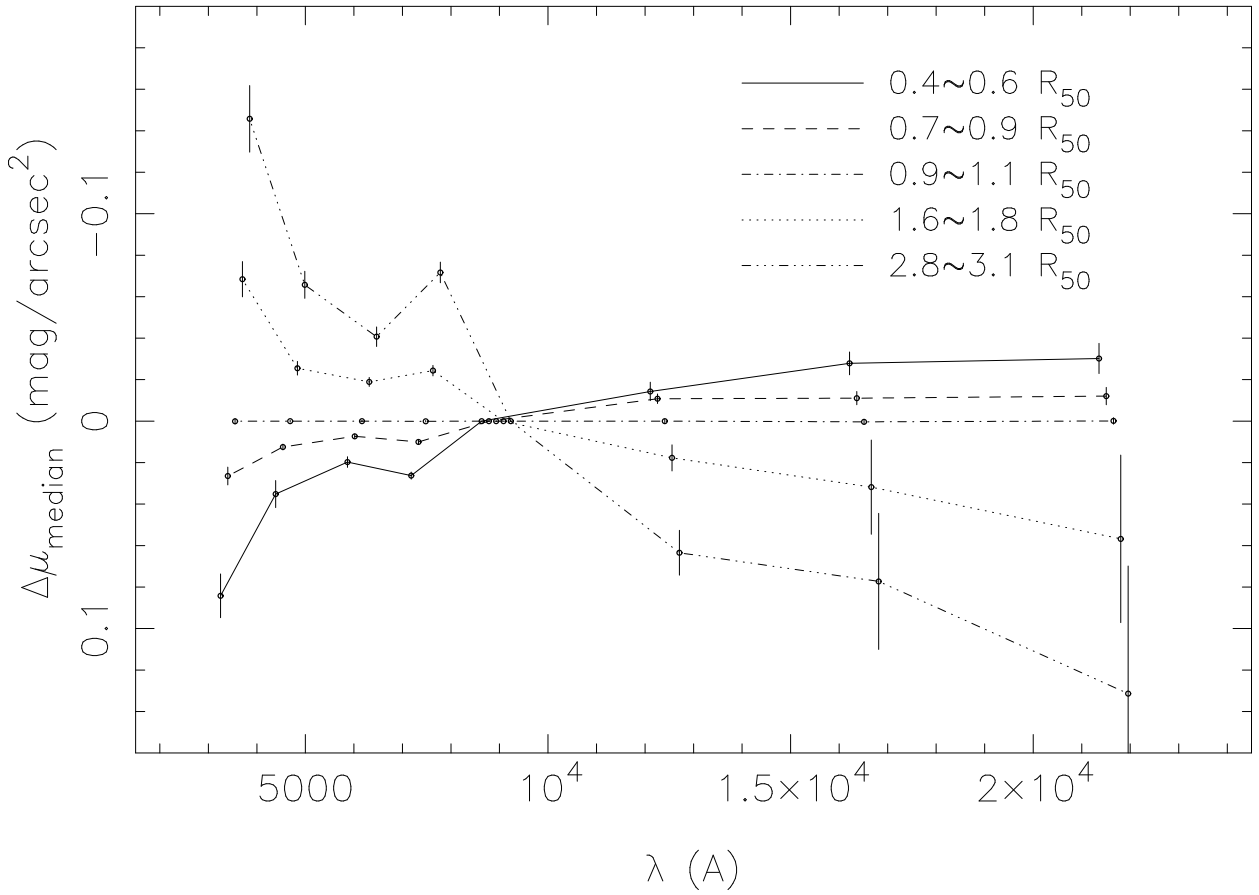


Fig. 4.— The relative shape of the SED at different radii. The plot shows the median values of $\Delta\mu = [\mu - \mu_z] - [\mu(R_{50}) - \mu_z(R_{50})]$ for the 35 sample galaxies at given bins of R/R_{50} , together with uncertainties. For clarity, wavelengths are shifted a bit for different radii.

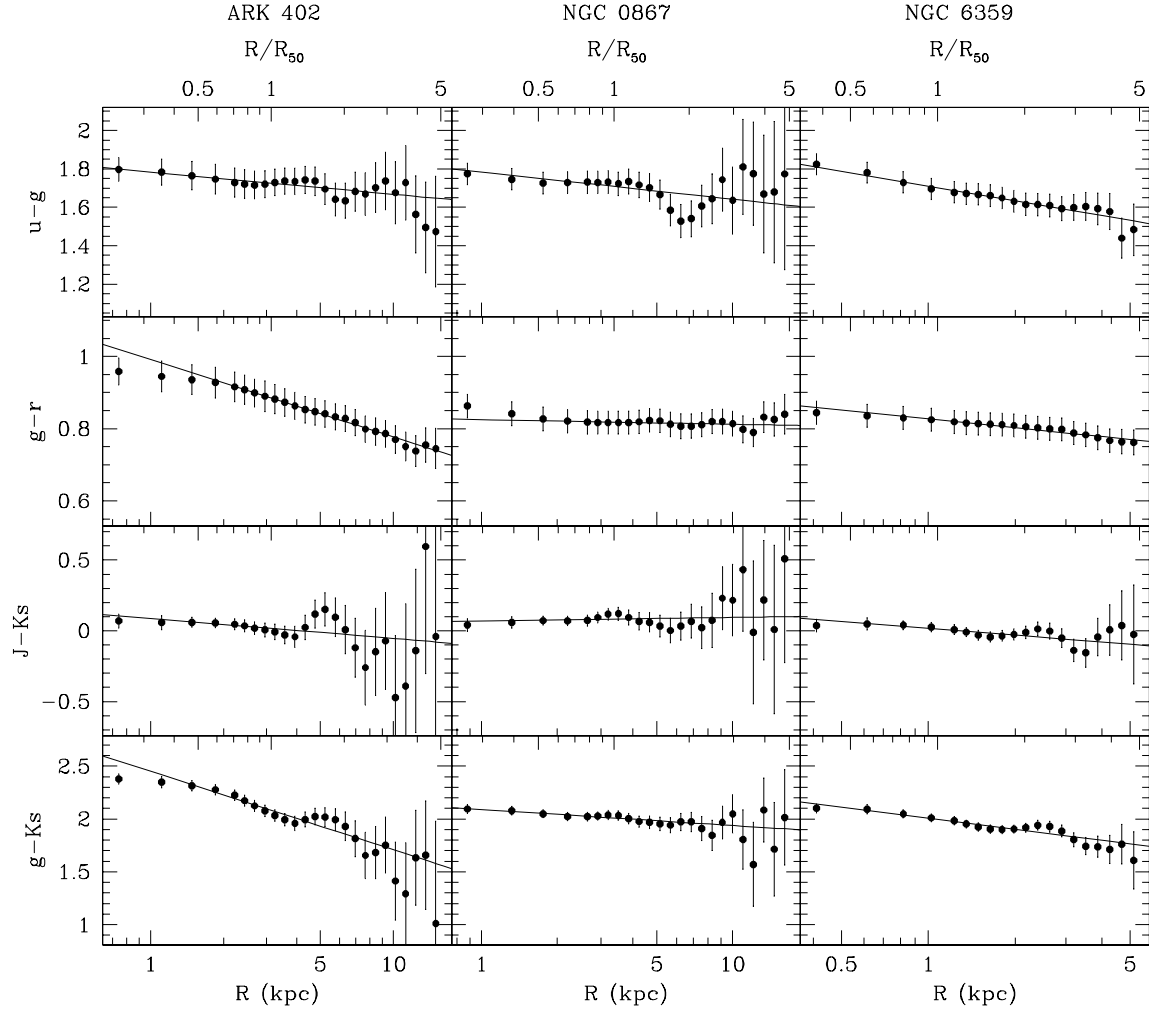


Fig. 5.— Examples of optical and near-infrared color profiles (color versus the radius of isophotic annulus) for galaxies Ark 402, NGC 0867, and NGC 6359. The line in each panel is the best fit to the color profile. The radius in units of R_{50} (the SDSS r -band) is also labelled for the corresponding galaxies.

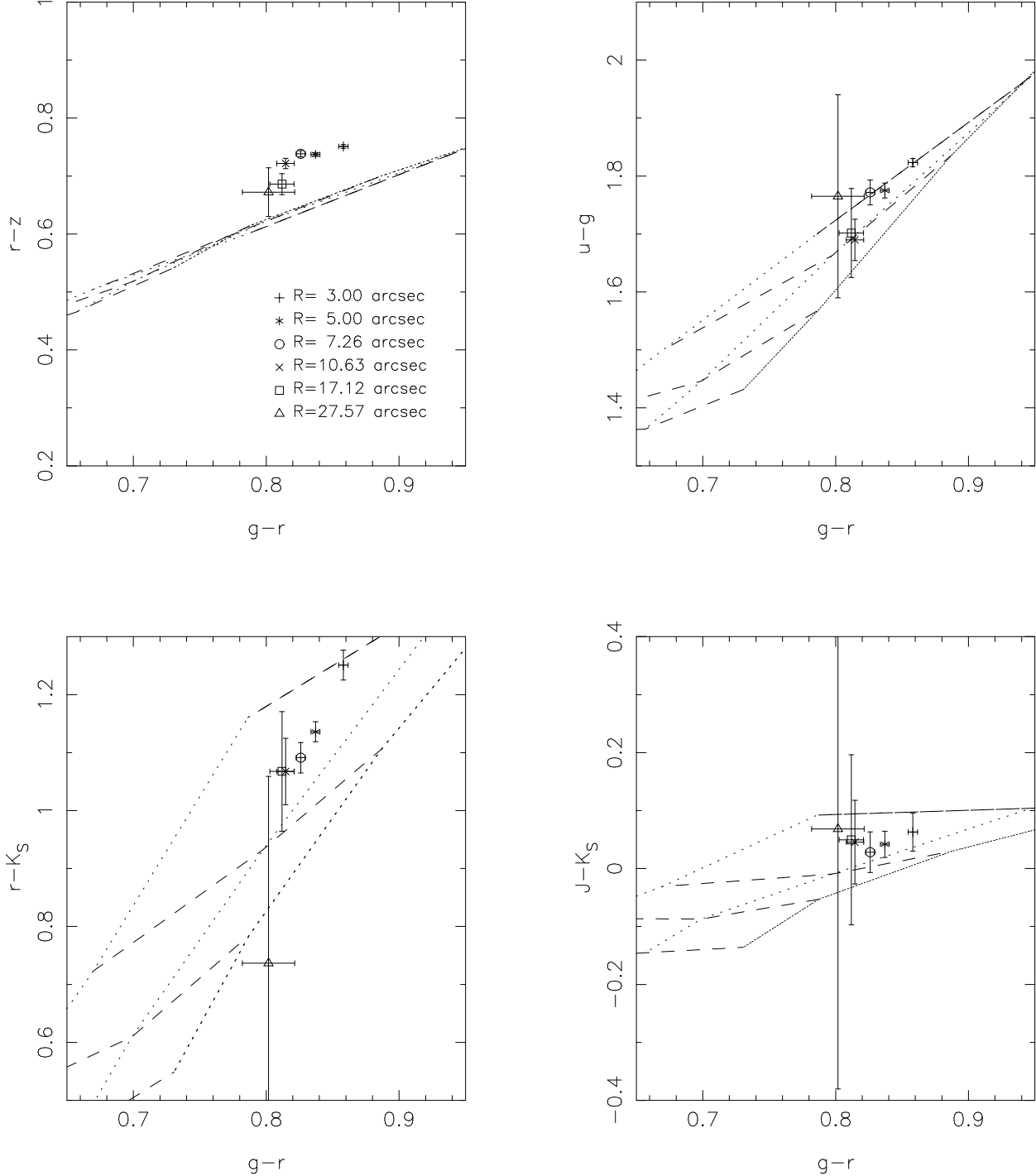


Fig. 6.— Color-color plots of NGC 4044. Different symbols with error bars are observational data at different radius. Grids are draw from SSP modal data, while dashed lines represent iso-metallicities colors, from down to up, they are 0.004, 0.008, 0.02 and 0.05, and dotted lines represent iso-ages ones of 2.0, 5.0 and 10.0 Gyrs from left to right.

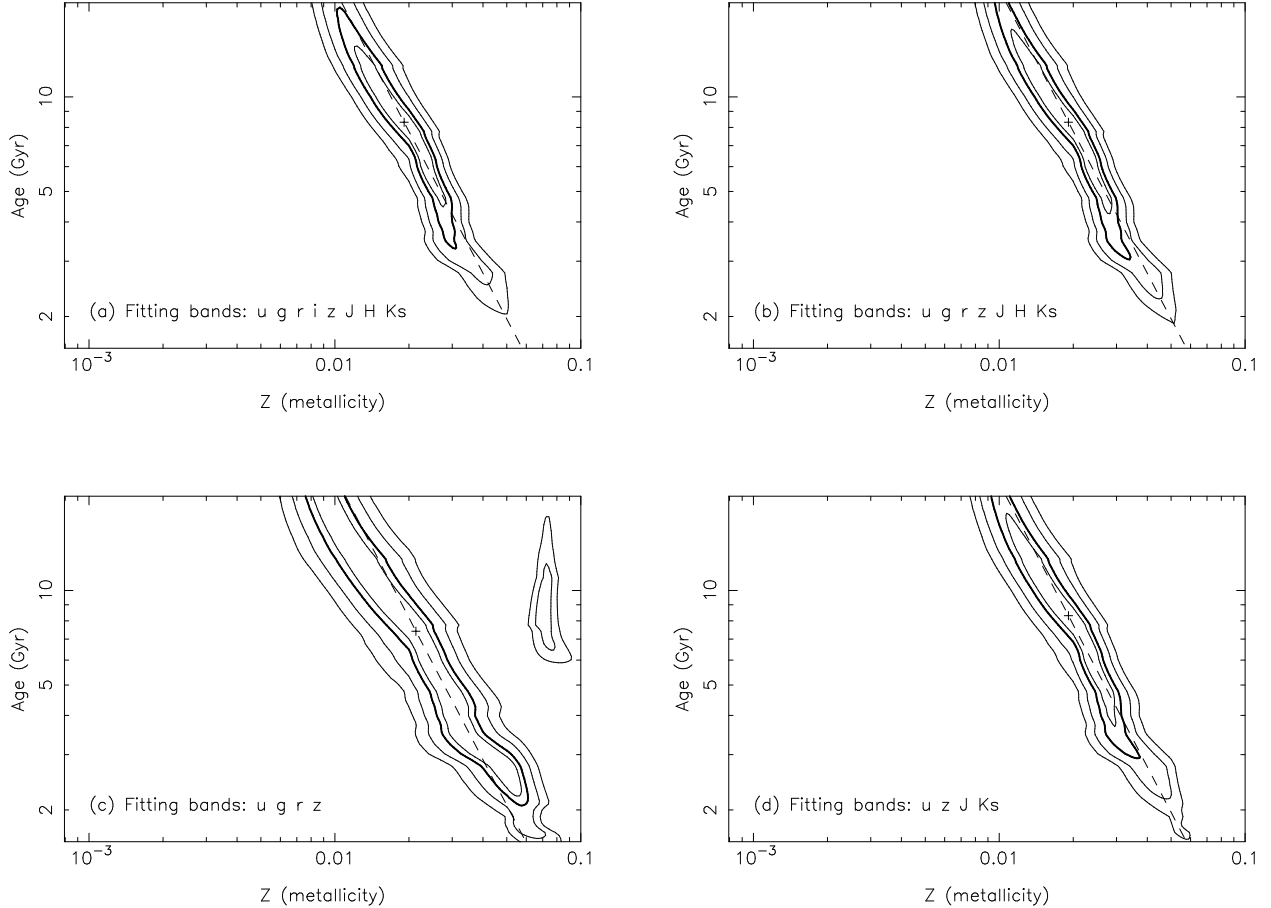


Fig. 7.— The contour s of $\Delta\chi^2$ for a simple stellar population with $\text{Age} = 8\text{Gyr}$ and $Z_{\text{met}} = 0.02(\sim Z_{\odot})$. Magnitude uncertainties in individual bands are chosen to be the typical values for our sample: $\sigma_{\text{obs}} = 0.03, 0.02, 0.02, 0.02, 0.02, 0.03, 0.04$, and 0.05 mag for the u , g , r , i , z , J , H , and K_{S} bands respectively. A model error of $\sigma_{\text{mod}} = 0.05$ mag was also included. The thick lines show $\Delta\chi^2 = 2.30$, which corresponds to the 68.3% confidence level, and the two outer contours correspond to the 95.4% and 99.7% confidence levels respectively. The innermost lines have $\Delta\chi^2 = 1.0$ which indicates the errors if only one of the parameters is fitted. Panel (a) shows the results obtained by using all eight bands of data; panel (b) uses all bands except i ; panel (c) uses only four SDSS bands (also excluding i); panel (d) uses four bands that cover both SDSS and 2MASS wavelengths. Dashed lines in these plots represent the $3/2$ age-metallicity degeneracy.

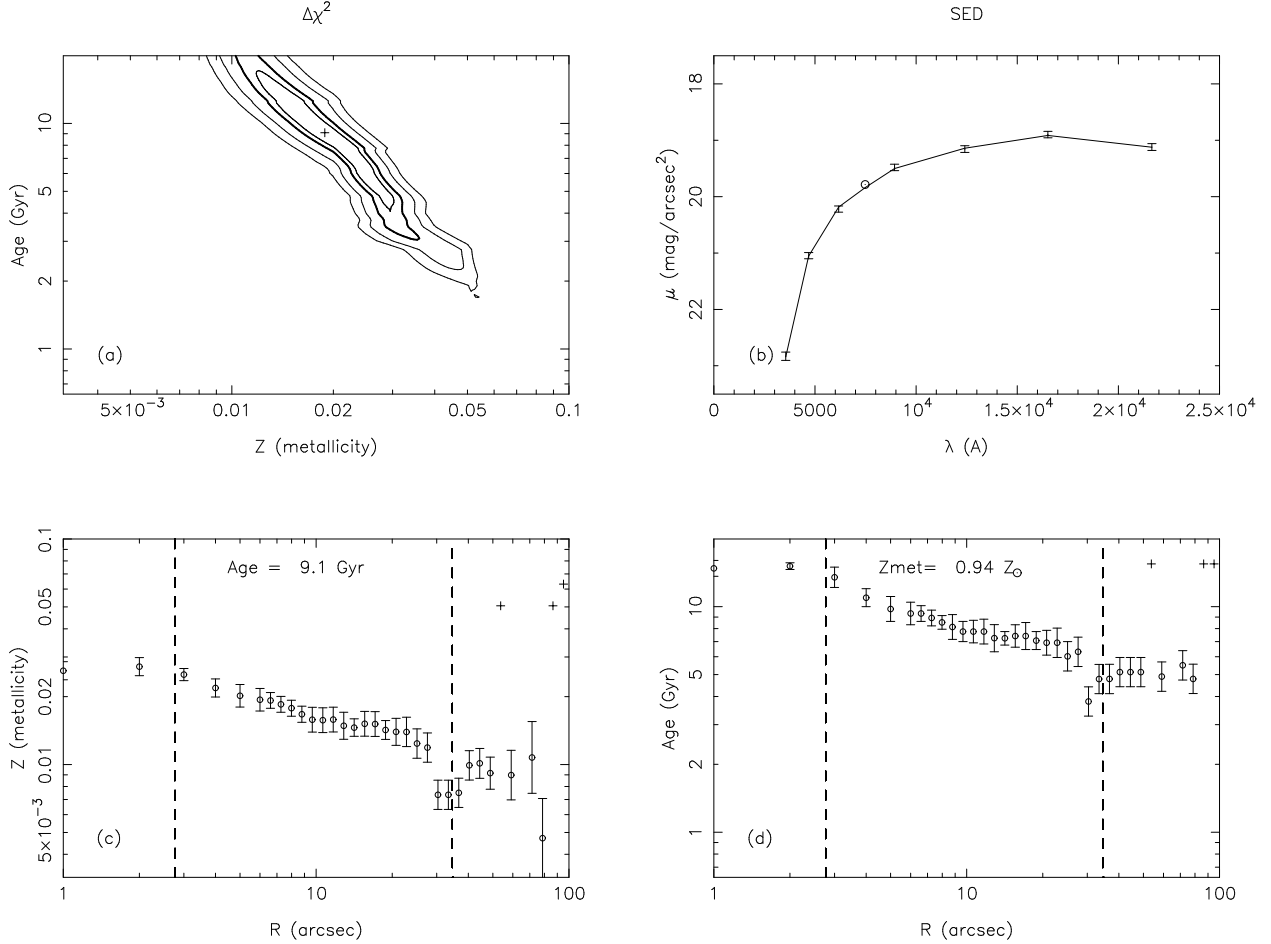


Fig. 8.— An example of the fit to the SED of NGC 4044. Panel (a) shows the contour map of $\Delta\chi^2$ for the fit of the SED at R_{50} ; panel (b) shows the best fit SED, with the line showing the SED for a SSP with $Z_{met} = 0.94 Z_\odot$ and Age = 9.1 Gyr. The omitted *i*-band data is plotted as a circle in this figure. Panel (c) presents the best fit Z_{met} values and their errors at different radii, where *Age* is forced to be the best fit value at R_{50} , i.e. 9.1 Gyr. Panel (d) shows the best fit age at different radii, where Z_{met} is forced to be the best fit value at R_{50} , i.e. $0.94 Z_\odot$. Crosses in panels (c) and (d) indicate the failure of fitting at these radii because the quality of the observations was too low to give a meaningful constraint.

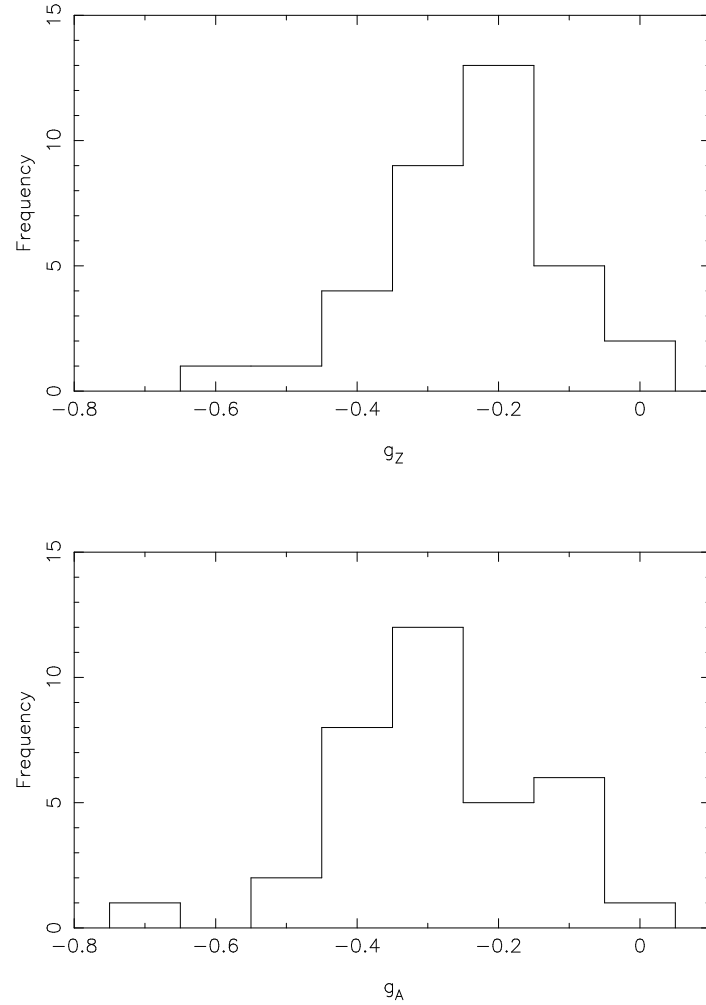


Fig. 9.— The distribution of metallicity gradients g_Z (upper panel, obtained assuming $g_A \equiv 0$) and age gradients g_A (lower panel, obtained assuming $g_Z \equiv 0$). The median values are $g_Z \approx -0.22$ and $g_A \approx -0.31$ for the two distributions.

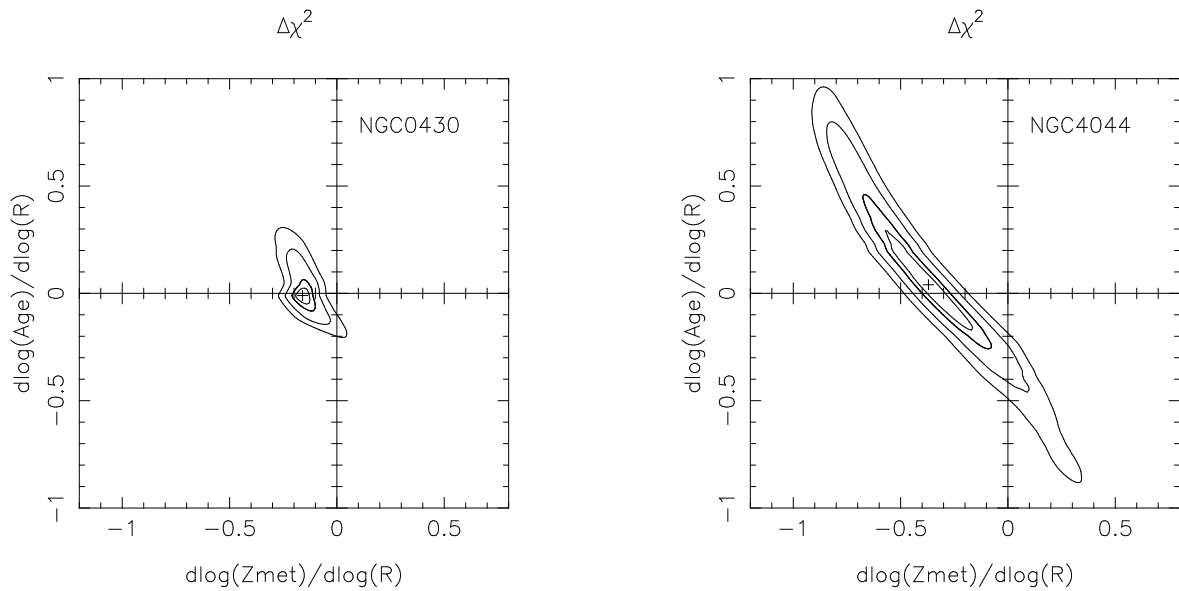


Fig. 10.— The $\Delta\chi^2$ contours in $g_Z - g_A$ space for NGC 0430 and NGC 4044. The thick lines have $\Delta\chi^2 = 2.30$, corresponding to a 68.3% confidence level while the two outer contours correspond to the 95.4% and 99.7% confidence levels respectively. The innermost lines have $\Delta\chi^2 = 1.0$ which indicates the errors if only one of the two parameters is fitted.

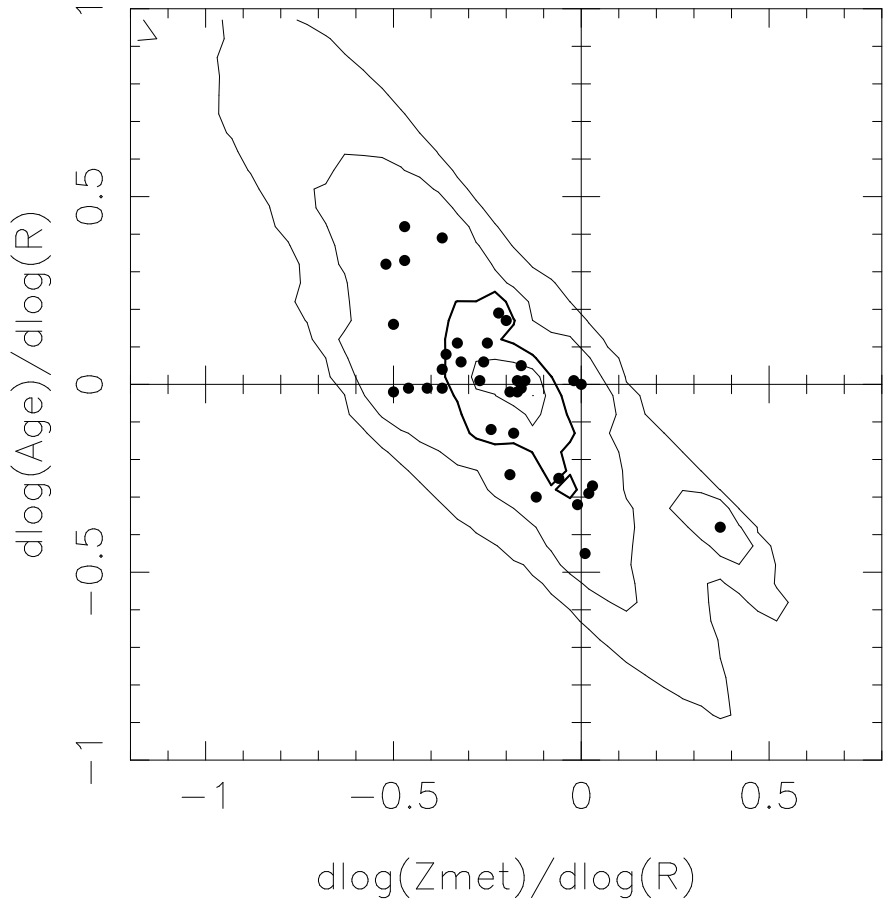


Fig. 11.— The distribution of g_Z and g_A obtained by fitting the observed SEDs with the SSP model. Solid points represent the best fit of individual galaxies. Contours show the relative number density of galaxies in this parameter space, and are obtained by summing up the probability distribution of each galaxy derived from its $\Delta\chi^2$ distribution (see figure 10). The thick line is the contour which encloses 68.3% of the total galaxy number, while the other two lines show the 95.4% and 99.7% confidence regions.

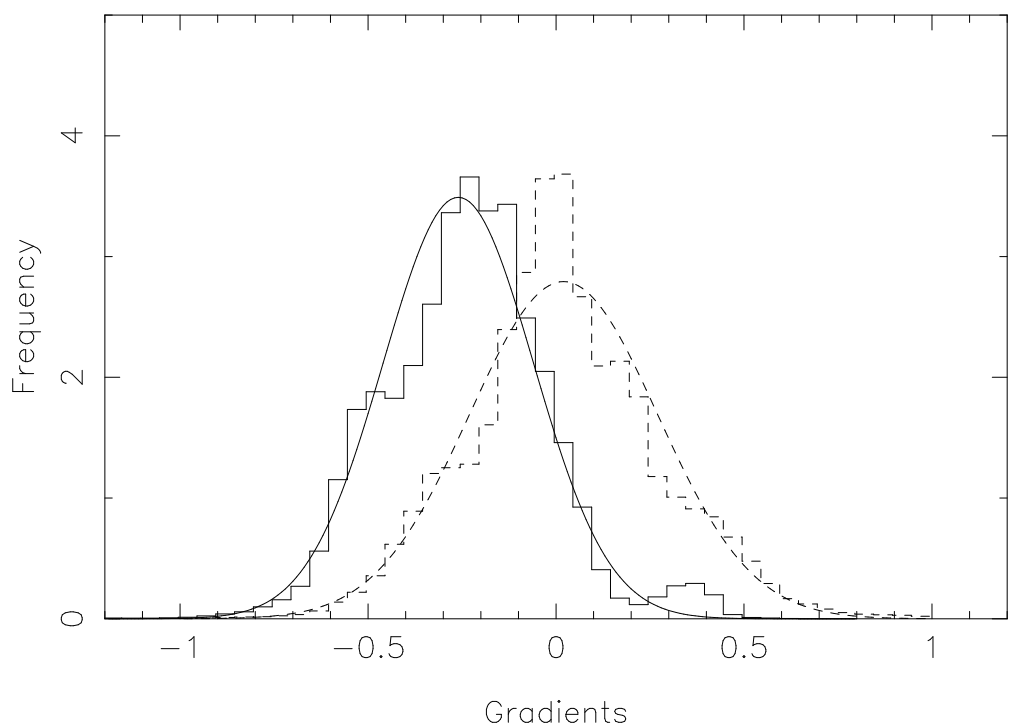


Fig. 12.— The projection of the two-dimensional contours shown in Figure 11 onto the g_Z (solid histogram) and g_A (dashed histogram) axes. The solid and dashed smooth curves show the best Gaussian fits.

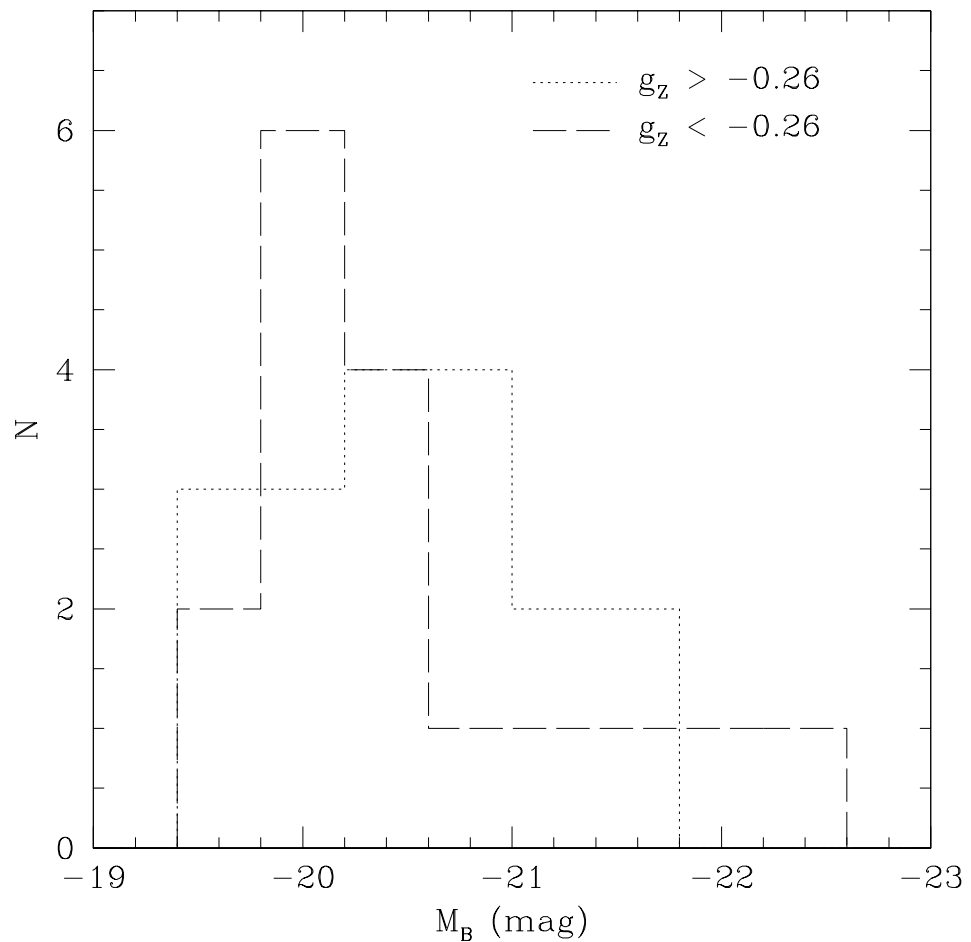


Fig. 13.— The distributions of absolute B magnitudes for the sample galaxies with g_Z above and below -0.26.

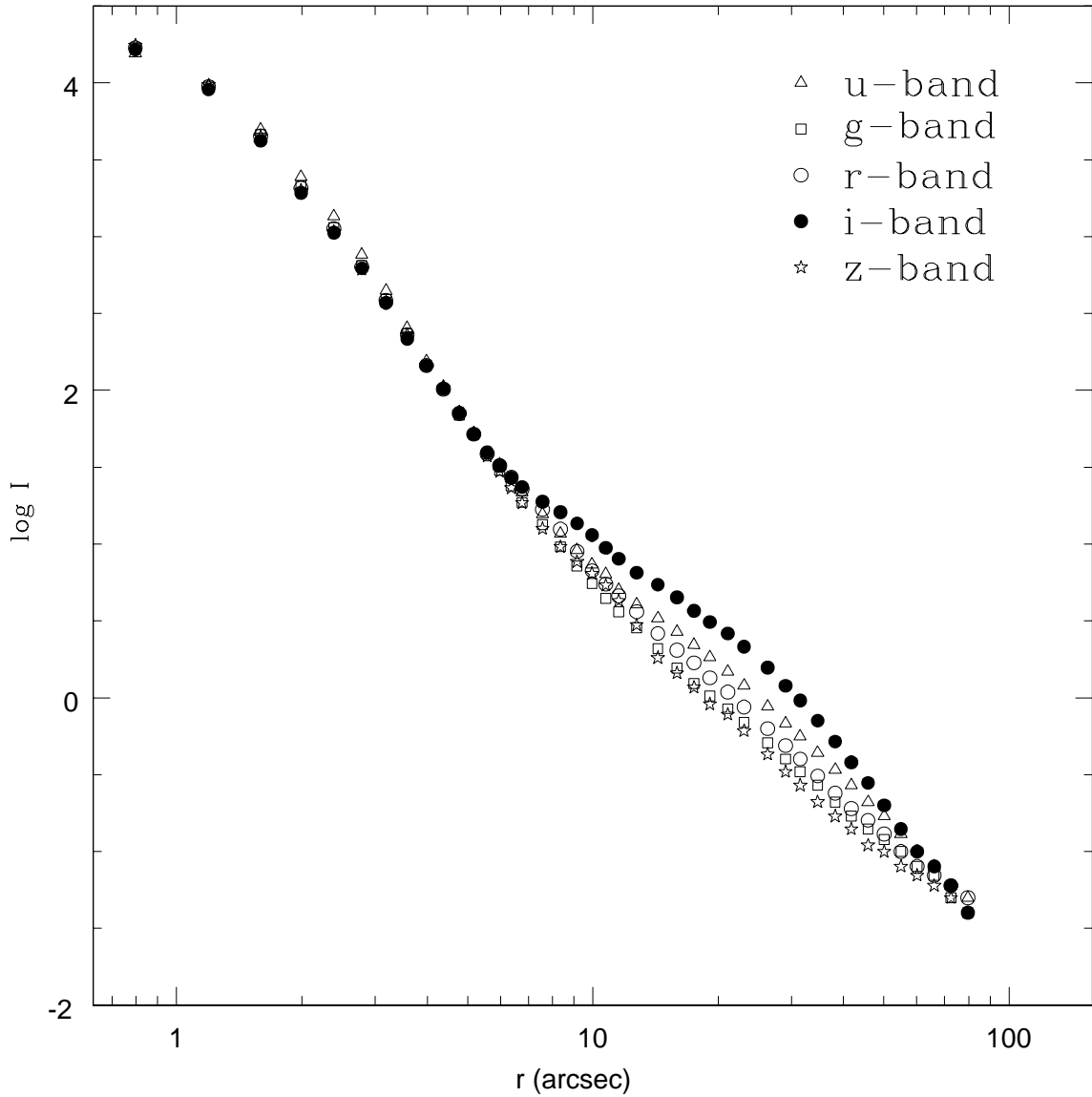


Fig. 14.— The radial profiles of the averaged PSFs in five SDSS bands. Each PSF profile is re-scaled and plotted with different symbols. The red halo of the PSF is clearly seen in the i -band. It produces a bright wing that is most prominent in the radius range $10''$ to $50''$.